Parametric Frequency Conversion of Resonance Radiation in Optically Pumped Rb^{87} Vapor*

Henry Tang

Columbia Radiation Laboratory, Department of Physics, Columbia University, New York, New York 10027

(Received 26 December 1972)

This paper reports an investigation of parametric frequency conversion in a vapor of Rb^{87} atoms in which nearly resonant optical waves are coupled with microwaves at the ground-state hyperfine-structure (hfs) frequency of Rb^{87} by the nonlinear susceptibilities of Rb^{87} vapor. These nonlinear susceptibilities are greatly enhanced by optical pumping of the ground-state hfs levels of Rb^{87} and by using nearly resonant light. The frequency-conversion process generates optical sideband waves which are separated in frequency from the carrier light waves by the ground-state hfs frequency of Rb^{87} (6.835 GHz). These sidebands have been directly observed in the spectral profiles of Rb^{85} resonance light which had passed through Rb^{87} vapor. The conversion efficiency of power from the carrier waves to the sideband waves in a 45-cm length of vapor was greater than 1%. The observed behavior of the sidebands is in excellent qualitative agreement with the predictions of a semiclassical theory.

I. INTRODUCTION

The index of refraction of an optically pumped vapor undergoing coherent magnetic resonance transitions can have components which oscillate in time at the magnetic resonance frequency. The effects of these oscillating indices of refraction on the propagation of light through the vapor were first observed in certain light-modulation experiments in optically pumped vapors. Following a suggestion by Dehmelt,[1] Bell and Bloom[2] observed that Na resonance light, which has passed through a vapor of optically pumped Na atoms, undergoing ground-state Zeeman transitions, was intensity modulated at the Zeeman frequency. A similar type of light-modulation experiment using K^{39} resonance light in a vapor of optically pumped K^{39} atoms undergoing ground-state hyperfine structure transitions (at 458 MHz) was performed by Firester and Carver.[3] Subsequently, Mathur *et al.*[4] used a newly developed crossed-field photomultiplier[5] tube to detect intensity modulation of Rb^{85} resonance light at the Rb^{87} ground-state hfs frequency (6.835 GHz). This latter experiment settled a controversy over whether, in this type of experiment, the light can be modulated at such high freqeuncies. The controversy was due in part to poor theoretical understanding of light-modulation experiments and in part to the lack of sensitive photodetectors with microwave bandwidths.

The basic difference between light-modulation experiments at microwave frequencies and those at lower radiofrequencies is that in the former, the transit time of the light through the vapor is comparable to or exceeds the period of oscillation of the applied microwave field. In this case, the extent of the modulation will depend on not only the size of the coupling susceptibility but also on how well the optical field, the microwave field, and the optical sideband field, which is generated, are phasematched. We have recently reported[6] on the direct observation of optical sidebands generated onto the spectral profile of a beam of Rb^{85} D_1-resonance light in a vapor of optically pumped Rb^{87} atoms undergoing ground-state hfs transitions. The sidebands could be easily observed because the spectral width of the Rb^{85} light (~1.5 GHz) was smaller than the ground-state hfs transition frequency of Rb^{87}, so that the sidebands were well resolved. Also, because a long length of Rb^{87} vapor was used, and the optical and microwave fields were kept well phasematched, the sidebands could be made quite intense. An additional feature of this experiment was that the long length of vapor which was used entirely absorbed the resonant portions of the probing light so that it was only possible to observe the sidebands generated from the off-resonance parts of the probing light.

In this paper, we present the results of a detailed experimental study of these parametric processes in optically pumped Rb^{87} vapor. We also present in Sec. II a semiclassical theory which predicted this effect.

II. THEORY

In this section, we first calculate the dielectric susceptibility of optically pumped Rb^{87} vapor with ground-state hfs coherence. Then we incorporate this susceptibility into Maxwell's equations and solve for wave-propagation solutions in the vapor. In the calculation for the susceptibility we make use of the formulas for the polarizability operator for Rb^{87} vapor derived in a paper by Mathur, Tang, and Happer,[7] which will hereafter be referred to as MTH. These formulas were derived using the effective operator formalism of Happer and Mathur,[8] whose paper we will hereafter refer to as HM.

A. Polarizability Operator

According to the theory of Happer and Mathur, the dielectric polarizability of an alkali vapor can be expressed as the expectation value of an appropriate polarizability operator $\overleftrightarrow{\alpha}$,[9]

$$\langle\overleftrightarrow{\alpha}\rangle = \mathrm{Tr}[\overleftrightarrow{\alpha}\rho], \tag{1}$$

where ρ is the ground-state density matrix of the vapor. The susceptibility $\langle\overleftrightarrow{\chi}\rangle$ of the vapor is defined as

$$\langle\overleftrightarrow{\chi}\rangle = N\langle\overleftrightarrow{\alpha}\rangle, \tag{2}$$

where N is the atomic density in the vapor. The polarizability operator for Rb^{87} vapor is given by MTH (39). According to that formula we can write the polarizability as a sum of four terms,

$$\langle\overleftrightarrow{\alpha}\rangle = \alpha_{eq}(\omega) + \alpha_{hfs}(\omega)\langle\vec{I}\cdot\vec{J}\rangle + i\sum_{FF'}\alpha_{gt}(F,F';\omega) \times\langle\vec{J}(F,F')\rangle\times + \sum_{FF'}\alpha_{br}(F,F';\omega)\langle\overleftrightarrow{Q}(F,F')\rangle. \tag{3}$$

All the terms in (3) except for the first term are proportional to some macroscopic observable of the vapor. The coefficients α in these terms are complex and are functions of the optical frequency, ω. The first term, α_{eq}, is the equilibrium polarizability, which is independent of the state of the vapor. The second term in (3) is the hyperfine polarizability, which is proportional to the quantity $\langle\vec{I}\cdot\vec{J}\rangle$, which is a measure of the ground-state hfs polarization. The third term in (3) contains the gyrotropic polarizabilities, which are proportional to the expectation value of the electronic angular momentum operator $\vec{J}(F,F')$. The symbol $\times$ in this term indicates a vector cross product. The fourth term in (3) is composed of the birefringent polarizabilities of the vapor, which are proportional to the expectation values of the quadrupole operator $\overleftrightarrow{Q}(F,F')$.

The energy levels of the ground state of Rb^{87} are shown in Fig. 1(a). Rb^{87} has a nuclear spin of $I=\frac{3}{2}$ so the hyperfine interaction splits its $^2S_{1/2}$ ground state into two hfs levels designated by total angular-momentum quantum numbers $F=1$ and $F=2$. In our experiment, a small static magnetic field (~ 2 g) is applied to remove the degeneracy of the magnetic sublevels so that the ground state is split into a total of eight Zeeman sublevels. Figure 1(b) shows a representation of the spectral profile of Rb^{85} D_1 light superimposed on the Rb^{87} absorption profiles. The hfs splitting of Rb^{85} (3.035 GHz) is smaller than that of Rb^{87} (6385 GHz). Nevertheless, the splitting is well resolved in the spectral profile of Rb^{85} D_1 light and the hfs components of Rb^{85}, which has a nuclear spin of $I=\frac{5}{2}$, are designated by $F=3$ and $F=2$. Owing to Doppler broadening, and the isotope shift, the

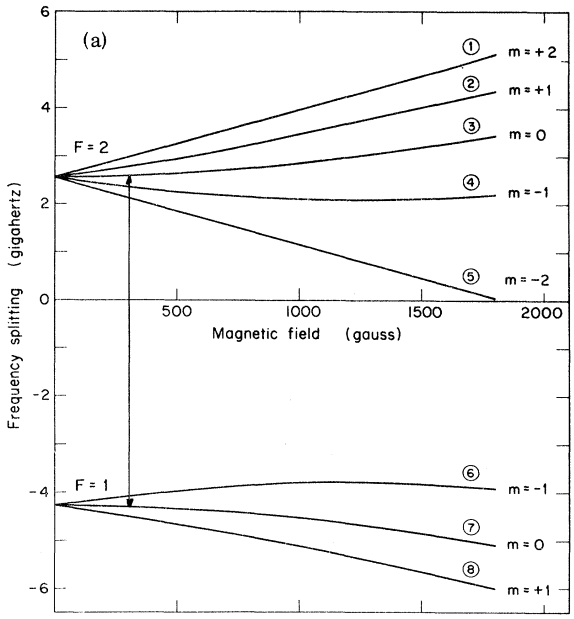

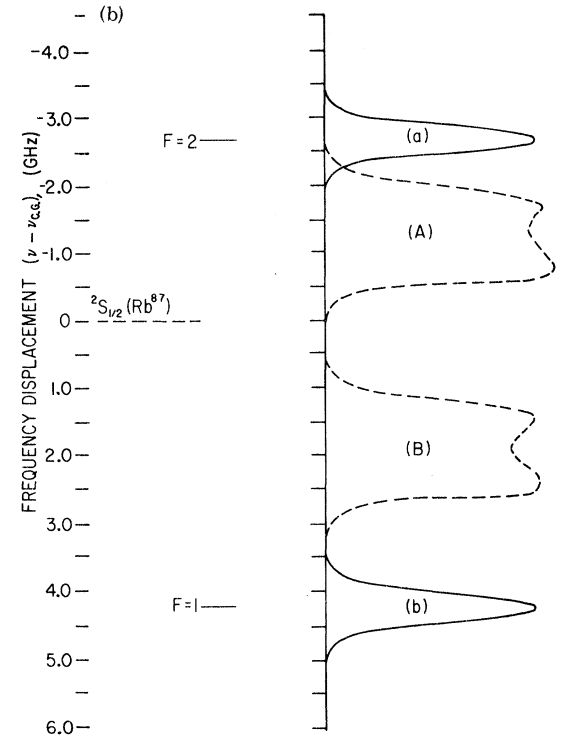

FIG. 1. (a) Energy levels of the $5\,^2S_{1/2}$ ground state of Rb^{87}. The "0-0" transition is indicated by arrows. (b) Components *a* and *b* represent the absorption line of Rb^{87} for the $5\,^2S_{1/2} \rightarrow 5\,^2P_{1/2}$ transition. Components *a* and *b* represent a typical spectral profile of D_1 light from a Rb^{85} lamp. *A* represents the $F=3$ hfs component while *B* represents the $F=2$ hfs component of the Rb^{85} light.

$F=3$ component of Rb^{85} light overlaps the $F=2$ component of the Rb^{87} absorption. We make use of this accidental overlap in our experiment by illuminating the Rb^{87} vapor with Rb^{85} resonance light. Thus, we were able to deplete the $F=2$ hfs level and produce an excess population into the $F=1$ hfs level. Having established a population imbalance in the hfs levels of Rb^{87} by optical pumping, a resonant microwave magnetic field parallel to the static field was applied to the vapor to excite the $|F=1;\ m_F=0\rangle$-to-$|F=2;\ m_F=0\rangle$ transition as indicated in Fig. 1(a). This transition will be, hereafter, referred to as the "0-0" transition. The combined effect of the optical pumping and the resonant microwave magnetic field is that the atoms in the vapor go into a coherent superposition of the two hfs levels, or we say that the vapor has acquired hfs coherence. The effect of the optical pumping on the polarizability of the vapor is to give it a nonvanishing hfs polarizability. The value of $\langle \vec{I}\cdot\vec{J}\rangle = -\frac{5}{4}$ when all the atoms are in the $F=1$ hfs level. One cannot usually pump all the atoms in the vapor into one hfs level so that in our case $\langle \vec{I}\cdot\vec{J}\rangle$ lies somewhere between 0 and $-\frac{5}{4}$. Since we have not affected the population distribution among the Zeeman levels in each hfs level, no static components of the gyrotropic or birefringent polarizability have been generated. However, because the vapor was undergoing coherent 0-0 transitions, the ground-state density matrix acquired nonvanishing oscillatory off-diagonal elements. This gives rise to two nonvanishing terms in the gyrotropic susceptibility (see Appendix A). One can also show (see Appendix B) that 0-0 hfs coherence gives no nonvanishing terms to the birefringent polarizability. Therefore, under the conditions we have stated, the polarizability of the Rb^{87} vapor can be written as

$$\langle \overleftrightarrow{\alpha}\rangle = \alpha_{eq}(\omega) + \alpha_{hfs}(\omega)\,\langle \vec{I}\cdot\vec{J}\rangle + (i/2)\,\alpha_{gt}(12;\omega) \times \langle 20|\rho|10\rangle \hat{e}_z \times + (i/2)\,\alpha_{gt}(21;\omega)\,\langle 10|\rho|20\rangle \hat{e}_z \times, \tag{4}$$

where $\langle 1,0|\rho|2,0\rangle$ and $\langle 2,0|\rho|1,0\rangle$ are off-diagonal elements of the ground-state density matrix, $\hat{e}_z$ is a unit vector in the direction of the static magnetic field which we will call the z direction, and we have substituted for the matrix elements of $\vec{J}$; $\langle 2,0|J|1,0\rangle = \langle 1,0|\vec{J}|2,0\rangle = -\frac{1}{2}e_z$ (see Appendix A).

B. Ground-State Density Matrix

The sublevels of the Rb^{87} ground state are numbered according to Fig. 1(a). Since the microwave field excites transitions only between levels 3 and 7, we will assume that the only nonvanishing off-diagonal elements of the density matrix are ρ_{37} and ρ_{73}. The density matrix of the eight sublevels can be written as

$$\begin{bmatrix} \rho_{11} & 0 & 0 & 0 & 0 & 0 & 0 & 0 \\ 0 & \rho_{22} & 0 & 0 & 0 & 0 & 0 & 0 \\ 0 & 0 & \rho_{33} & 0 & 0 & 0 & \rho_{37} & 0 \\ 0 & 0 & 0 & \rho_{44} & 0 & 0 & 0 & 0 \\ 0 & 0 & 0 & 0 & \rho_{55} & 0 & 0 & 0 \\ 0 & 0 & 0 & 0 & 0 & \rho_{66} & 0 & 0 \\ 0 & 0 & \rho_{73} & 0 & 0 & 0 & \rho_{77} & 0 \\ 0 & 0 & 0 & 0 & 0 & 0 & 0 & \rho_{88} \end{bmatrix}. \tag{5}$$

The time rate of change of any element of (5) is governed by the equation

$$\frac{d\rho}{dt} = \frac{1}{i\hbar}\left[(\mathcal{H}_0+\mathcal{H}_{rf}),\rho\right] + \frac{1}{i\hbar}\left[\delta\mathcal{H}\rho - \rho\delta\mathcal{H}^{\dagger}\right] + \left(\frac{\partial\rho}{\partial t}\right)_{repop} + \left(\frac{\partial\rho}{\partial t}\right)_{relax}, \tag{6}$$

where $\mathcal{H}_0$ is the unperturbed Hamiltonian of the atoms, $\mathcal{H}_{rf}$ describes the effect of the applied microwave magnetic field, $\delta\mathcal{H}$ is a non-Hermitian effective Hamiltonian[10] which describes the effect of the optical-pumping light. The term $(\partial\rho/\partial t)_{repop}$ accounts for the rate of repopulation of the ground-state sublevels owing to spontaneous decay from the excited states, and $(\partial\rho/\partial t)_{relax}$ accounts for the return to thermal equilibrium of the populations of the sublevels and of the coherences between these levels.

Writing the first term on the left side of (6) in component form as

$$\frac{1}{i\hbar}\left[\mathcal{H}_0,\rho\right]_{\alpha\alpha'} = \frac{1}{\hbar}\left(\rho_{\alpha\alpha'}E_{\alpha'} - \rho_{\alpha\alpha'}E_{\alpha}\right), \tag{7}$$

we find that under the conditions we have assumed for the experiment, the only nonvanishing components of (7) are

$$\frac{1}{i\hbar}\left[\mathcal{H}_0,\rho\right]_{37} = -i\omega_0\rho_{37} \tag{8}$$

and

$$\frac{1}{i\hbar}\left[\mathcal{H}_0,\rho\right]_{73} = i\omega_0\rho_{73}, \tag{9}$$

where $\omega_0 = (E_3 - E_7)/\hbar$.

If we let the frequency of the applied microwave field be Ω, then we can write the microwave field $\vec{H}$ in the form

$$\vec{H}(\Omega) = \vec{H}_1\cos\Omega t. \tag{10}$$

Then $\mathcal{H}_{rf}$ can be written as

$$\mathcal{H}_{rf} = g_J\mu_B\vec{J}\cdot\vec{H}_1\cos\Omega t. \tag{11}$$

The term $(1/i\hbar)[\mathcal{H}_{rf},\rho]$ can be written in component form as

$$\frac{1}{i\hbar}[\mathcal{H}_{rf},\rho]_{\alpha\alpha'}=\frac{i}{\hbar}\sum_k g_J\mu_B H_1\cos\Omega t \times[\rho_{\alpha k}\langle k|J_x|\alpha'\rangle-\langle\alpha|J_x|k\rangle\rho_{k\alpha'}]. \quad (12)$$

By substituting $\langle 7|J_x|3\rangle=\langle 3|J_x|7\rangle=-\frac{1}{2}$ and dropping the rapidly oscillating terms, we write the nonvanishing components of (12) as

$$\frac{1}{i\hbar}[\mathcal{H}_{rf},\rho]_{33}=2\beta\,\mathrm{Im}\rho_{73}e^{-i\Omega t}, \quad (13a)$$

$$\frac{1}{i\hbar}[\mathcal{H}_{rf},\rho]_{77}=-2\beta\,\mathrm{Im}\rho_{73}e^{-i\Omega t}, \quad (13b)$$

$$\frac{1}{i\hbar}[\mathcal{H}_{rf},\rho]_{73}=-i\beta(\rho_{77}-\rho_{33})e^{i\Omega t}, \quad (13c)$$

and

$$\frac{1}{i\hbar}[\mathcal{H}_{rf},\rho]_{37}=i\beta(\rho_{77}-\rho_{33})e^{-i\Omega t}, \quad (13d)$$

where $\beta=\mu_B H_1/2\hbar$.

The effective Hamiltonian $\delta\mathcal{H}$ according to HM (2.37) is expressible in terms of two Hermitian operators, $\delta\mathcal{E}$ and $\delta\Gamma$,

$$\delta\mathcal{H}=\delta\mathcal{E}-i\hbar(\delta\Gamma/2)=-\vec{\mathcal{E}}^*\cdot\overleftrightarrow{\alpha}\cdot\vec{\mathcal{E}}, \quad (14)$$

where $\delta\mathcal{E}$ is the light-shift operator defined by HM (2.38) and $\delta\Gamma$ is the light absorption operator defined by HM (2.39). The term $(1/i\hbar)[\delta\mathcal{H}\rho-\rho\delta\mathcal{H}^\dagger]$ in (6) may be written in component form as

$$\frac{1}{i\hbar}[\delta\mathcal{H}\rho-\rho\delta\mathcal{H}^\dagger]_{\alpha\alpha'}=\sum_k\left[\frac{i}{\hbar}(\rho_{\alpha k}\langle k|\delta\mathcal{E}|\alpha'\rangle-\langle\alpha|\delta\mathcal{E}|k\rangle\rho_{k\alpha'})-\tfrac{1}{2}(\langle\alpha|\delta\Gamma|k\rangle\rho_{k\alpha'}+\rho_{\alpha k}\langle k|\delta\Gamma|\alpha'\rangle\right]. \quad (15)$$

The diagonal matrix elements of $\delta\mathcal{E}$ account for shifts of the ground-state energy levels owing to the light,[11] while the diagonal matrix elements of $\delta\Gamma$ account for the excitation of atoms[12] from the ground state to the excited state. The off-diagonal matrix elements of $\delta\mathcal{E}$ and $\delta\Gamma$ contribute only at zero magnetic field or when the light is intensity modulated.[13,14] Otherwise, those terms may be neglected, and (15) becomes

$$\frac{1}{i\hbar}[\delta\mathcal{H}\rho-\rho\delta\mathcal{H}^\dagger]_{\alpha\alpha'}=-\left[\tfrac{1}{2}\langle\alpha'|\delta\Gamma|\alpha'\rangle-\frac{i}{\hbar}\langle\alpha'|\delta\mathcal{E}|\alpha'\rangle\right]\rho_{\alpha\alpha'}-\left[\tfrac{1}{2}\langle\alpha|\delta\Gamma|\alpha\rangle+\frac{i}{\hbar}\langle\alpha|\delta\mathcal{E}|\alpha\rangle\right]\rho_{\alpha\alpha'}. \quad (16)$$

Since the optical-pumping light (Rb^{85} resonance light) excites Rb^{87} atoms out of only the $F=2$ hfs level of the ground state [see Fig. 1(b)] we can write[15]

$$\langle\alpha|\delta\Gamma|\alpha\rangle=0 \quad \text{for } \alpha=6,7,8, \quad (17a)$$

and

$$\langle\alpha|\delta\Gamma|\alpha\rangle=\Gamma \quad \text{for } \alpha=1,2,3,4,5, \quad (17b)$$

where Γ is defined as the optical-pumping rate expressed in photons absorbed per atom per second. Since we shall be exciting magnetic resonance transitions between levels 3 and 7 we need only be concerned with the light shifts of these two levels. We write

$$(1/\hbar)[\langle 3|\delta\mathcal{E}|3\rangle-\langle 7|\delta\mathcal{E}|7\rangle]=\Delta\omega_l, \quad (18)$$

where $\Delta\omega_l$ is defined as the light shift in radians per second of the transition frequency between levels 3 and 7. We now write for the components of (16)

$$(1/i\hbar)[\delta\mathcal{H}\rho-\rho\delta\mathcal{H}^\dagger]_{\alpha\alpha}=-\Gamma\rho_{\alpha\alpha} \quad \text{for } \alpha=1,2,3,4,5, \quad (19a)$$

$$(1/i\hbar)[\delta\mathcal{H}\rho-\rho\delta\mathcal{H}^\dagger]_{73}=[-\tfrac{1}{2}\Gamma+i\Delta\omega_l]\rho_{73}, \quad (19b)$$

and

$$(1/i\hbar)[\delta\mathcal{H}\rho-\rho\delta\mathcal{H}^\dagger]_{37}=[-\tfrac{1}{2}\Gamma-i\Delta\omega_l]\rho_{37}. \quad (19c)$$

We shall assume that repopulation of the eight ground-state sublevels occurs with equal probability; so we write

$$\left(\frac{d\rho_{\alpha\alpha}}{dt}\right)_{\text{repop}}=\tfrac{1}{8}\Gamma(\rho_{11}+\rho_{22}+\rho_{33}+\rho_{44}+\rho_{55}) \quad \text{for } \alpha=1-8. \quad (20)$$

This last assumption will be valid if a buffer gas at a sufficiently high pressure is present in the resonance cell to collisionally depolarize the excited states of the Rb^{87} atoms.

Ground-state relaxation of alkali atoms due to spin exchange,[16,17] buffer-gas collisions,[18] and diffusion to the walls[19] is exceedingly complicated, although a great deal is known about it. However, to account for all presently known aspects of ground-state relaxation in detail would introduce so many mathematical complexities that it would obscure the basically simple analysis of the light propagation. We therefore represent the ground-state relaxation with the following simplified equations, which, while not strictly correct, nevertheless reproduce the important qualitative properties of the relaxation:

$$\left(\frac{d\rho_{\alpha\alpha}}{dt}\right)_{\text{relax}}=-\gamma_1(\rho_{\alpha\alpha}-\tfrac{1}{8}) \quad \text{for } \alpha=1-8, \quad (21a)$$

$$\left(\frac{d\rho_{73}}{dt}\right)_{\text{relax}}=-\gamma_2\rho_{73}, \quad (21b)$$

and

$$\left(\frac{d\rho_{37}}{dt}\right)_{\text{relax}} = -\gamma_2 \rho_{73}. \tag{21c}$$

On combining (8), (9), (13), (17)–(21), and recognizing that $\rho_{11}=\rho_{22}=\rho_{44}=\rho_{55}$ and $\rho_{66}=\rho_{88}$, we obtain the following set of equations for the elements of (5):

$$\frac{d\rho_{22}}{dt} = -\Gamma\rho_{22} + \tfrac{1}{8}\Gamma(4\rho_{22}+\rho_{33}) - \gamma_1(\rho_{22}-\tfrac{1}{8}), \tag{22a}$$

$$\frac{d\rho_{33}}{dt} = -\Gamma\rho_{33} + \tfrac{1}{8}\Gamma(4\rho_{22}+\rho_{33}) - \gamma_1(\rho_{33}-\tfrac{1}{8}) + 2\beta\,\mathrm{Im}\rho_{73}e^{-i\Omega t}, \tag{22b}$$

$$\frac{d\rho_{66}}{dt} = \tfrac{1}{8}\Gamma(4\rho_{22}+\rho_{33}) - \gamma_1(\rho_{66}-\tfrac{1}{8}), \tag{22c}$$

$$\frac{d\rho_{77}}{dt} = \tfrac{1}{8}\Gamma(4\rho_{22}+\rho_{33}) - \gamma_1(\rho_{77}-\tfrac{1}{8}) - 2\beta\,\mathrm{Im}\rho_{73}e^{-i\Omega t}, \tag{22d}$$

$$\frac{d\rho_{73}}{dt} = i\omega_0\rho_{73} - i\beta(\rho_{77}-\rho_{33})e^{i\Omega t} - [\tfrac{1}{2}\Gamma+\gamma_2]\rho_{73} + i\Delta\omega_l\rho_{73}, \tag{22e}$$

$$\frac{d\rho_{37}}{dt} = i\omega_0\rho_{37} + i\beta(\rho_{77}-\rho_{33})e^{-i\Omega t} - [\tfrac{1}{2}\Gamma+\gamma_2]\rho_{37} - i\Delta\omega_l\rho_{37}. \tag{22f}$$

On comparing (22e) and (22f) we can see that $\rho_{37}=\rho_{73}^{*}$. To obtain the steady-state value of ρ_{37} we let

$$\rho_{37} = \sigma e^{-i\Omega t}, \tag{23}$$

and substitute in (22f) to give

$$\sigma = \frac{-\beta(\rho_{77}-\rho_{33})}{(\Omega-\omega_0-\Delta\omega_l)+i[(1/2)\Gamma+\gamma_2]}. \tag{24}$$

By equating the left side of (22a)–(22d) to zero, we can solve for the steady-state value of $(\rho_{77}-\rho_{33})$ to give

$$(\rho_{77}-\rho_{33}) = \frac{\tfrac{1}{8}\Gamma\gamma_1(\Gamma+\gamma_1)}{[\tfrac{3}{8}\Gamma^2\gamma_1+\tfrac{11}{8}\Gamma\gamma_1^2+\gamma_1^3]+[\tfrac{1}{4}\Gamma^2+\tfrac{7}{4}\Gamma\gamma_1+2\gamma_1^2]2\beta^2\epsilon}, \tag{25}$$

where

$$\epsilon = \frac{[\tfrac{1}{2}\Gamma+\gamma_2]}{(\Omega-\omega_0-\Delta\omega_l)^2+[\tfrac{1}{2}\Gamma+\gamma_2]^2}. \tag{26}$$

From (23) and (24) we note that the off-diagonal density matrix elements of "coherences" exist when there is a population imbalance between levels 3 and 7 and when a resonant or nearly resonant microwave field induces transitions between these two levels. Furthermore, the coherences are oscillating in time at the frequency of the applied microwaves. Consequently, the gyrotropic components of the vapor polarizability in (4), which are proportional to the coherences, are oscillating at the microwave frequency. A plot of $|\rho_{37}|$ versus the magnitude of the microwave field $|\vec{H}_1|$ is shown in Fig. 2. In this figure the microwave frequency was taken to be on resonance ($\Omega=\omega_0+\Delta\omega_l$), and the vapor parameters were chosen to be representative of actual experimental conditions. We note in Fig. 2 that for small values of $|\vec{H}_1|$, $|\rho_{37}|$ varies linearly with $|\vec{H}_1|$. $|\rho_{37}|$ attains a maximum for some value of the field, and for large values of the field, the transition $3\rightarrow 7$ saturates and $|\rho_{37}|$ goes to zero. A plot of $|\rho_{37}|$ versus the microwave frequency Ω is shown in Fig. 3. Figure 3(a) shows the case of low microwave field $[4\beta^2 \ll (\tfrac{1}{2}\Gamma+\gamma_2)]$. We note that $|\rho_{37}|$ shows a normal resonance line shape, whereas, in Fig. 3(b) which shows the case when the microwave field is large $[4\beta^2 \gg (\tfrac{1}{2}\Gamma+\gamma_2)]$, $|\rho_{37}|$ decreases at the center of the resonance owing to saturation of the transition $3\rightarrow 7$. Therefore, we would expect the optical sideband amplitudes, which are roughly proportional to $|\rho_{37}|$, to have the same behavior with microwave field strength and microwave frequency as is illustrated in Figs. 2 and 3.

C. Steady-State Susceptibility of Rb^{87} Vapor

Using the expression for the off-diagonal density matrix elements derived in (23) and (24) in (4) and using the relation given by (2) we obtain the complete susceptibility for Rb^{87} vapor with 0-0 hfs coherence. This susceptibility can be separated into a static part and a part which oscillates at the driving microwave frequency. The static part χ_0 can be written as

$$\chi_0 = N[\alpha_{\text{eq}}(\omega)+\alpha_{\text{hfs}}(\omega)\langle\vec{I}\cdot\vec{J}\rangle]. \tag{27}$$

The explicit expressions for the complex coefficients $\alpha_{\text{eq}}(\omega)$ and $\alpha_{\text{hfs}}(\omega)$ for Rb^{87} vapor are found in MTH (41) and (42). A plot of the real part of χ_0 versus the optical frequency ω in the region near the D_1 transition of Rb^{87} is shown in Fig. 4. Figure 4(a) shows the case when the vapor has no hfs polarization ($\langle\vec{I}\cdot\vec{J}\rangle=0$), while Fig. 4(b) shows the case when there is a sizable excess population in the lower ($F=1$) ground-state hfs level. In general, the degree of hfs polarization depends on the pumping-light intensity, the atomic density, and the buffer-gas pressure. Therefore, the static susceptibility of the vapor will depend on these parameters.

The oscillating part of the Rb^{87}-vapor susceptibility may be written as

$$\langle\overleftrightarrow{\chi}_{\text{osc}}\rangle = \frac{i}{4}(\rho_{77}-\rho_{33})N\mu_B\left\{\frac{\alpha_{gt}(12;\omega)H_1e^{-i\Omega t}\hat{e}_z\times}{(\Omega-\omega_0-\Delta\omega_l)+i[\tfrac{1}{2}\Gamma+\gamma_2]} + \frac{\alpha_{gt}(21;\omega)H_1e^{i\Omega t}\hat{e}_z\times}{(\Omega-\omega_0-\Delta\omega_l)-i[\tfrac{1}{2}\Gamma+\gamma_2]}\right\}. \tag{28}$$

The explicit expressions for the coefficients $\alpha_{gt}(12;\omega)$ and $\alpha_{gt}(21;\omega)$ for Rb^{87} are found in MTH (53). A plot of $\alpha_{gt}(12;\omega)$ and $\alpha_{gt}(21;\omega)$ versus optical

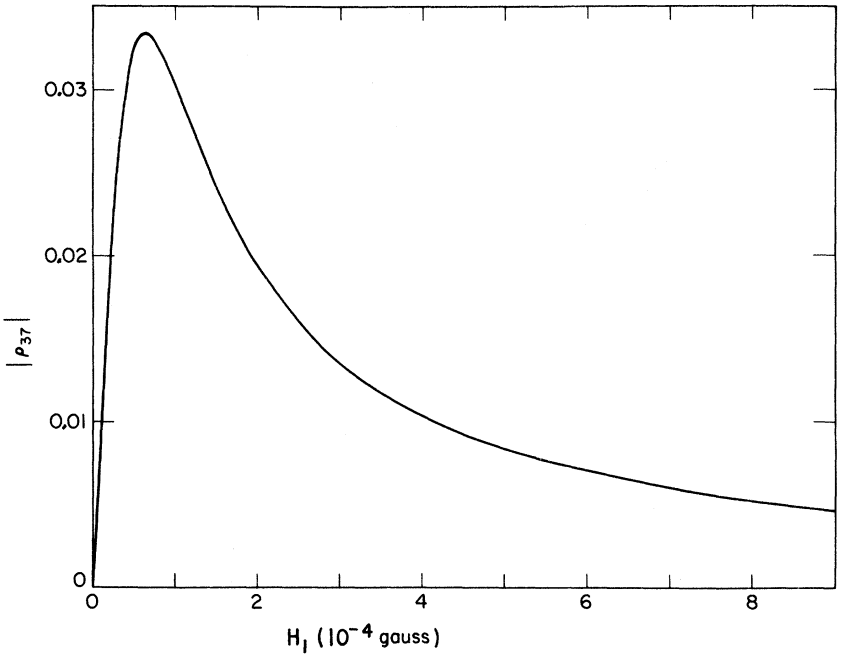

FIG. 2. $|\rho_{37}|$ vs the magnitude of the microwave field H_1. The vapor parameters were assumed to be $\Gamma = 10^3$ sec^{-1}; $\gamma_1 = 360$ sec^{-1}, $\gamma_2 = 230$ sec^{-1}.

frequency ω in the region near the D_1 transition of Rb^{87} is shown in Fig. 5.

D. Wave Propagation

Let us represent the electric field of a quasi-monochromatic-light wave by

$$\vec{E}(\vec{r}, t, \omega) = \vec{\mathcal{E}}(\zeta, t, \omega) e^{i[\vec{k}\cdot\vec{r} - \omega t]} + \text{c. c.}, \tag{29}$$

where c. c. denotes complex conjugate, and ζ is the distance along the direction of propagation,

$$\zeta = (1/k)\vec{k}\cdot\vec{r}. \tag{30}$$

The amplitude $\vec{\mathcal{E}}(\zeta, t, \omega)$ is a slowly varying function of and t. One can think of an incoherent light beam as a superposition of many monochromatic waves, such as (29) with various frequencies and random phases.

The wave (29) will induce dielectric polarization $\vec{P}$ in the Rb^{87} vapor,

$$\vec{P} = \langle\overleftrightarrow{\chi}\rangle \cdot \vec{\mathcal{E}}(\zeta, t, \omega) e^{i(\vec{k}\cdot\vec{r} - \omega t)} + \text{c. c.} \tag{31}$$

The static part of the susceptibility will generate a component of polarization which oscillates at the same frequency ω as the incident light wave. However, the two terms of the oscillating susceptibility will generate components of polarization which oscillate at frequencies $\omega + \Omega$ and $\omega - \Omega$. We will adopt terminology commonly used by radio engineers and call the light wave at frequency ω the carrier and the light waves at $\omega + \Omega$ and $\omega - \Omega$ the upper and lower sidebands, respectively. We can write the Cartesian components of the upper sideband polarization $P_i(\omega_+)$ as

$$P_i(\omega_+) = \sum_j \chi_{ij}(\omega_+ = \Omega + \omega) H(\Omega) E_j(\omega), \tag{32}$$

where ω_+ is the upper-sideband frequency and $\chi_{ij}(\omega_+ = \Omega + \omega)$ is a component of the up-coupling susceptibility.

We will keep in mind that both the static and microwave magnetic fields are oriented along the z direction. On comparing (32) with the first term in (28) we find that the only nonvanishing components of the up-coupling susceptibility are

$$\chi_{yx}(\omega_+ = \Omega + \omega) = -\chi_{xy}(\omega_+ = \Omega + \omega), \tag{33}$$

where

$$\chi_{yx}(\omega_+ = \Omega + \omega) = \frac{i}{4} \frac{N\mu_B(\rho_{77} - \rho_{33})\alpha_{gt}(12;\omega)}{(\Omega - \omega_0 - \Delta\omega_l) + i[\frac{1}{2}\Gamma + \gamma_2]}. \tag{34}$$

Similarly, we can show that the only nonvanishing components of the down-coupling susceptibility are

$$\chi_{yx}(\omega_- = -\Omega + \omega) = -\chi_{xy}(\omega_- = -\Omega + \omega), \tag{35}$$

where

$$\chi_{yx}(\omega_- = -\Omega + \omega) = \frac{i}{4} \frac{N\mu_0(\rho_{77} - \rho_{33})\alpha_{gt}(21;\omega)}{(\Omega - \omega_0 - \Delta\omega_l) - i[\frac{1}{2}\Gamma + \gamma_2]}. \tag{36}$$

From the forms of the nonvanishing components of the coupling susceptibilities of (34) and (36) we note that when the carrier light is linearly polarized, the sidebands will also be linearly polarized but in an orthogonal direction. If, however, the carrier light is circularly polarized, then the sidebands are also circularly polarized and in the same sense as the carrier. In the latter case, the carrier waves and the sideband waves mix, causing intensi-

ty beats in the light. These light beats have been observed in the experiments of Firester and Carver[20] and Mathur *et al.*[21]

To predict the behavior of the electric fields of the carrier and sidebands we must incorporate the carrier and sideband polarizations as source terms in Maxwell's equations. The wave equation for the electric field can be written as

$$\nabla\times\nabla\times\vec{E}-\frac{1}{c^2}\frac{\partial^2\vec{E}}{\partial t^2}=-\frac{4\pi}{c^2}\frac{\partial^2\vec{P}}{\partial t^2}\,. \tag{37}$$

By making the assumptions that the amplitudes

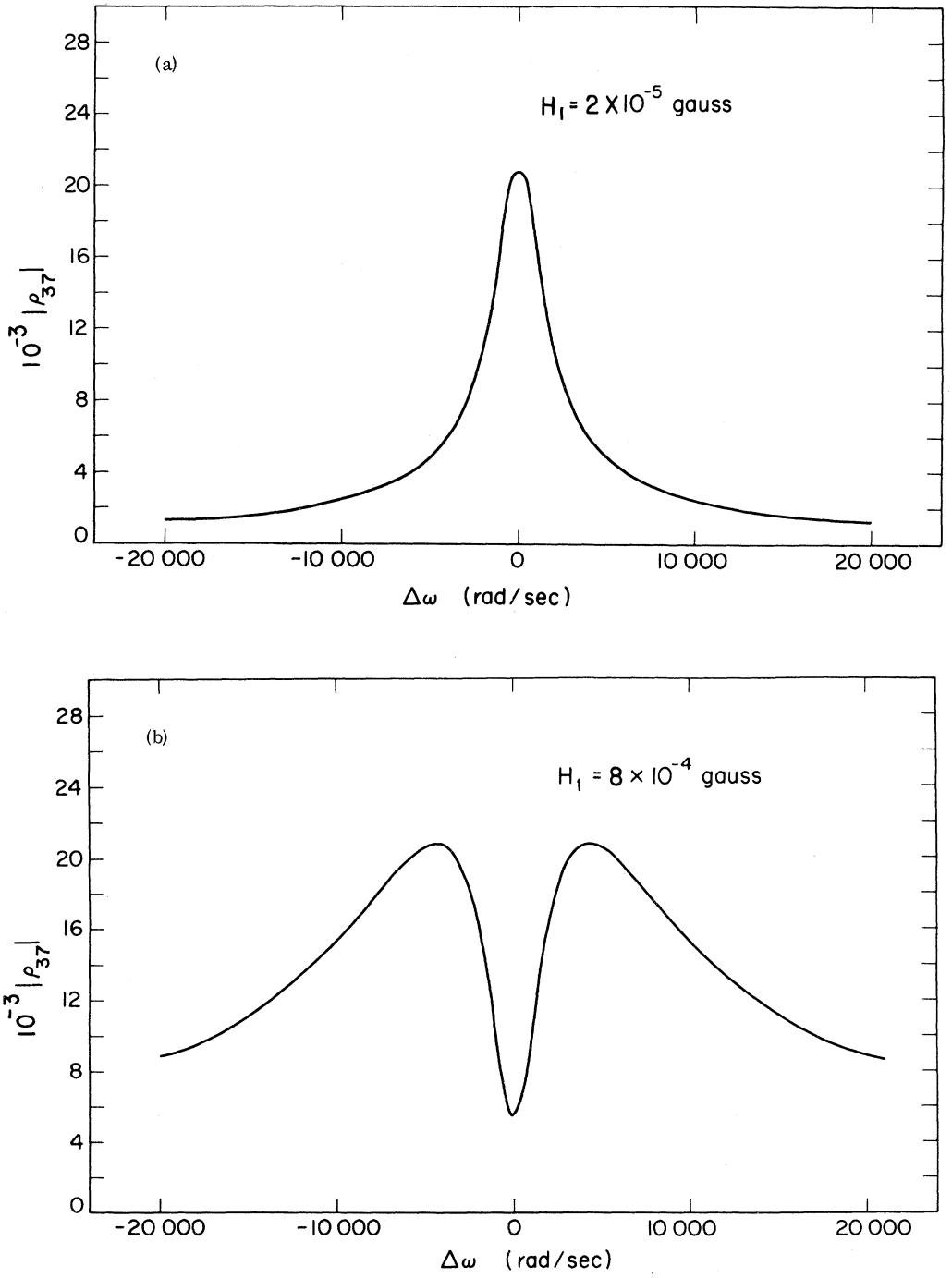

FIG. 3. (a) $|\rho_{37}|$ vs the microwave frequency for low microwave field. (b) $|\rho_{37}|$ vs the microwave frequency for high microwave field. The vapor parameters were assumed to be $\Gamma=10^3$ sec^{-1}, $\gamma_1=360$ sec^{-1}, $\gamma_2=230$ sec^{-1}.

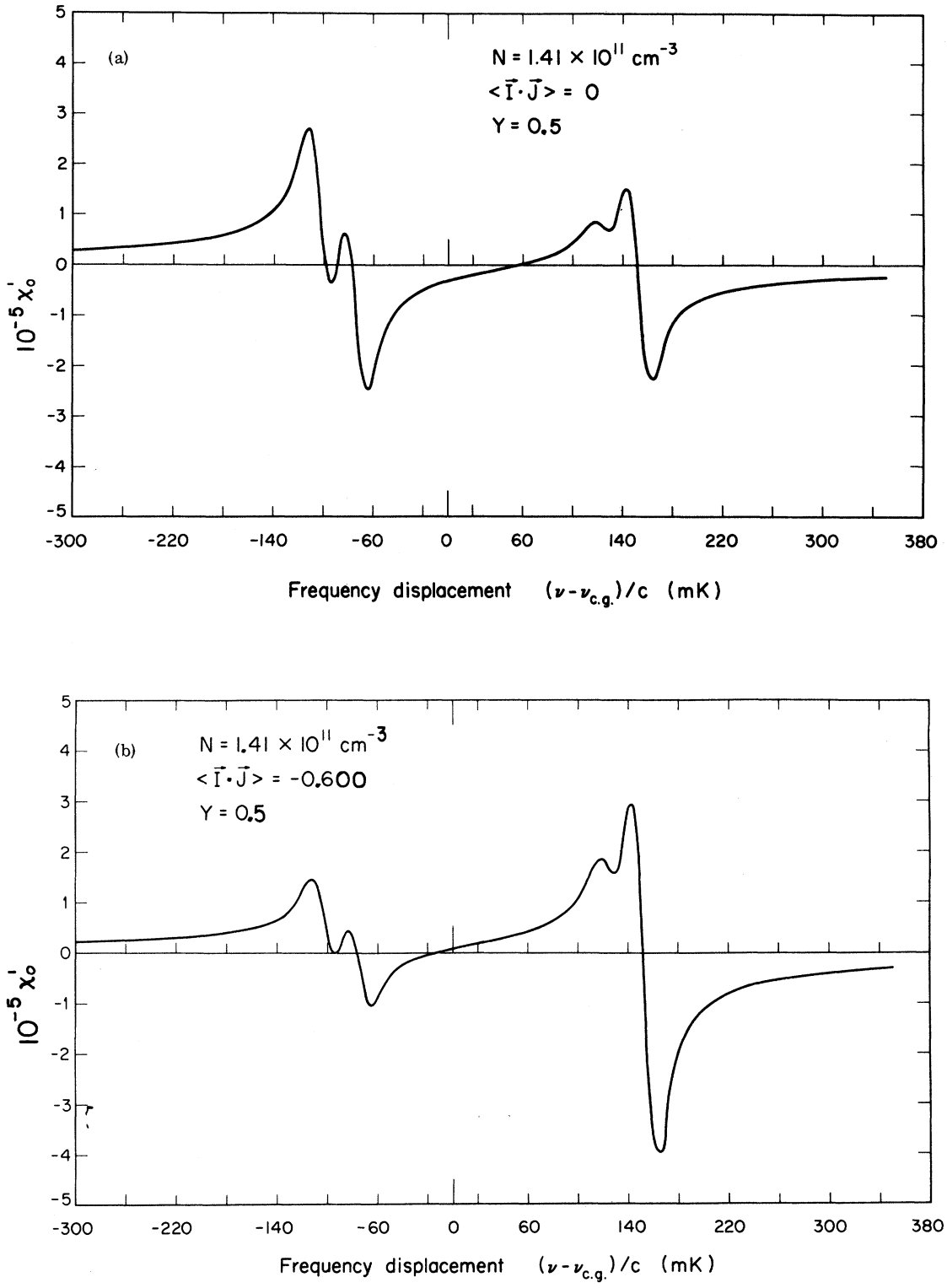

FIG. 4. (a) $\chi_0'(\omega)$ vs ω for D_1 light for the case of no hfs polarization. $\chi_0'(\omega) = \mathrm{Re}\chi_0(\omega)$. (b) $\chi_0'(\omega)$ vs ω for D_1 light for the case with hfs polarization. N is the atomic density which was taken to be that of a saturated rubidium vapor at 70 °C. Y is the broadening parameter to account for the buffer-gas-collision broadening of the optical-absorption line. See Ref. 7 for details of this calculation.

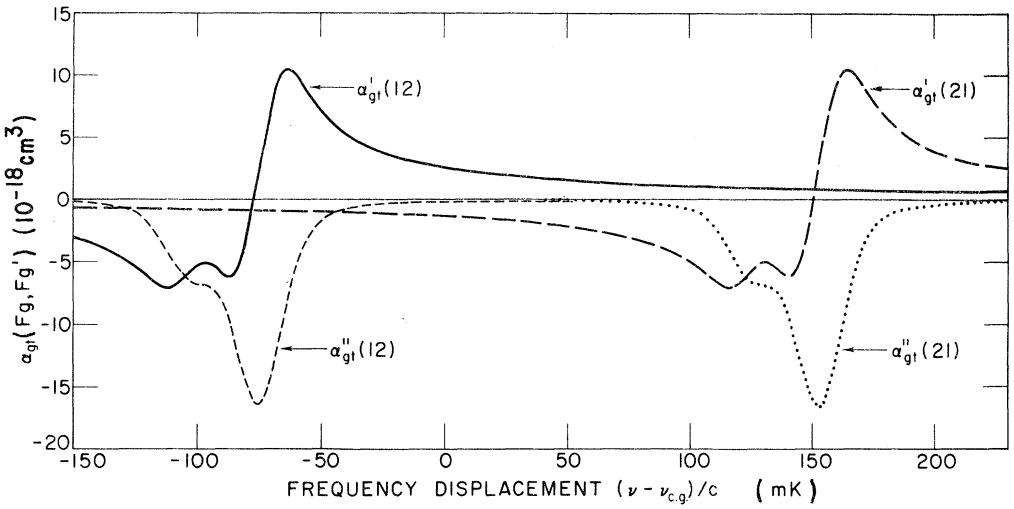

FIG. 5. $\alpha_{gt}(12;\omega)$ and $\alpha_{gt}(21;\omega)$ vs ω for D_1 light. See Ref. 7 for details of this calculation. $\alpha'_{gt}=\mathrm{Re}\alpha_{gt}$, $\alpha''_{gt}=\mathrm{Im}\alpha_{gt}$.

of the electric fields are slowly varying functions of time and distance one can show that Eq. (37) can be reduced to

$$\frac{\partial\vec{\mathcal{E}}(\zeta,t,\omega)}{\partial\zeta}+\frac{1}{c}\frac{\partial\vec{\mathcal{E}}(\zeta,t,\omega)}{\partial t}=\frac{2\pi i}{\omega c}\frac{\partial^2\vec{P}(r,t,\omega)}{\partial t^2}e^{-i(\vec{k}\cdot\vec{r}-\omega t)},\quad(38)$$

where $\vec{\mathcal{E}}(\omega)$ is the amplitude of the electric field at frequency ω as defined by (29). The polarization can be written in the form

$$\vec{P}(r,t,\omega)=\vec{\mathcal{P}}(\zeta,t,\omega)e^{i(\vec{k}\cdot\vec{r}-\omega t)}+\text{c.c.}\quad(39)$$

Substituting (39) into (38), we obtain

$$\left(\frac{\partial}{\partial\zeta}+\frac{1}{c}\frac{\partial}{\partial t}\right)\vec{\mathcal{E}}(\zeta,t,\omega)=2\pi ik\vec{\mathcal{P}}(\zeta,t,\omega).\quad(40)$$

In general, (40) represent an infinite set of coupled equations. But if we refer to Fig. 5, which shows the dependence of the coupling susceptibilities on optical frequency, we see that $\alpha_{gt}(12;\omega)$, which is the frequency-response function for the up-coupling susceptibility, is large only in the vicinity of the $F=2$ component of the Rb^{87} D_1 transition, and it goes to zero for higher and lower frequencies. Similarly, $\alpha_{gt}(21;\omega)$, which is the frequency response function for the down-coupling susceptibility, is large only in the vicinity of the $F=1$ component of the D_1 transition, and it also goes to zero for higher and lower frequency. It should also be noted that the imaginary parts of $\alpha_{gt}(12;\omega)$ and $\alpha_{gt}(21;\omega)$ are nonzero only on resonance. Therefore, the imaginary parts of the coupling susceptibilities are not useful in generating sidebands because the portions of the carrier-light spectral profile which are on resonance suffer strong absorption by the vapor. The real parts of the coupling susceptibilities, however, remain sizable even off resonance. Therefore, because the coupling susceptibilities are strongly frequency dependent we can assume that a monochromatic carrier wave couples efficiently only to an upper and a lower sideband. This assumption reduces the number of equations given by (40) to three. The expression for the microwave field given by (10) is for a field which is stationary in space. In our experiment, the interaction of light and microwaves occur over an extended region. The microwave field is applied by means of a resonant cavity whose axis is parallel to the light beam. The TE modes of this cavity have components of magnetic field which are parallel to the cavity axis. In the cavity, the fields are standing-wave fields which can be thought of as being composed of two oppositely directed traveling-wave fields. We will only consider the case of a traveling microwave field which propagates in the same direction as the light, and we will assume that the microwave field propagating in the opposite direction is badly phase matched so that it can be neglected. Hence, for the above case we can write the longitudinal component of the microwave magnetic field in the cavity in the form

$$\vec{H}(z,t,\Omega)=\vec{H}_1(\Omega)e^{i(Kz-\Omega t)}+\text{c.c.},\quad(41)$$

where $\vec{K}$ is the guide wave vector of the microwaves in the cavity. There will also be radial components of the microwave magnetic field in the cavity which we will ignore. We have also assumed in (41) that the amplitude of the microwave field remains constant. One can show that when the microwave field is of the form of (41) the coupling susceptibilities need only be modified by multiplying (34) by $e^{i(Kz)}$, and (36) by $e^{-i(Kz)}$. We can now write the com-

ponents of the polarization at the upper-sideband, the carrier, and the lower-sideband frequencies, assuming that the carrier wave is linearly polarized in the x direction and propagates in the z-direction as

$$P_y(\omega_+) = \mathcal{P}_y(\omega_+)\, e^{i(k_+ z-\omega_+ t)} + \text{c.c.}$$
$$= \chi_0(\omega_+)\mathcal{E}_y(\omega_+)\, e^{i(k_+ z-\omega_+ t)}$$
$$+ \chi_{yx}(\omega_+ = \Omega+\omega)\, H_1(\Omega)\, e^{i(Kz-\Omega t)}\mathcal{E}_x(\omega)\, e^{i(kz-\omega t)} + \text{c.c.}, \quad (42a)$$

$$P_x(\omega) = \mathcal{P}_x(\omega)\, e^{i(kz-\omega t)} + \text{c.c.}$$
$$= \chi_0(\omega)\mathcal{E}_x(\omega)\, e^{i(kz-\omega t)}$$
$$+ \chi_{xy}(\omega = -\Omega+\omega_+)\, H_1(\Omega)\, e^{-i(Kz-\Omega t)}\mathcal{E}_y(\omega_+)\, e^{i(k_+ z-\omega_+ t)}$$
$$+ \chi_{xy}(\omega = \Omega+\omega_-)\, H_1(\Omega)\, e^{i(Kz-\Omega t)}\mathcal{E}_y(\omega_-)\, e^{i(k_- z-\omega_- t)} + \text{c.c.}, \quad (42b)$$

$$P_y(\omega_-) = \mathcal{P}_y(\omega_-)\, e^{i(k_- z-\omega_- t)} + \text{c.c.}$$
$$= \chi_0(\omega_-)\mathcal{E}_y(\omega_-)\, e^{i(k_- z-\omega_- t)}$$
$$+ \chi_{yx}(\omega_- = -\Omega+\omega)\, H_1(\Omega)\, e^{-i(Kz-\Omega t)}\mathcal{E}_x(\omega)\, e^{i(kz-\omega t)} + \text{c.c.}, \quad (42c)$$

where $k_+ = \omega_+/c$ and $k_- = \omega_-/c$. By substituting (42) into the wave equation of (40) we arrive at the following set of coupled equations:

$$\frac{d}{dz}\mathcal{E}_y(\omega_+) = 2\pi ik\,[\chi_0(\omega_+)\mathcal{E}_y(\omega_+) + \chi_{yx}(\omega_+ = \Omega+\omega)\, H_1(\Omega)\mathcal{E}_x(\omega)\, e^{i\Delta Kz}], \quad (43a)$$

$$\frac{d}{dz}\mathcal{E}_x(\omega) = 2\pi ik\,[\chi_0(\omega)\mathcal{E}_x(\omega) + \chi_{xy}(\omega = \Omega+\omega_-)\, H_1(\Omega) \times \mathcal{E}_y(\omega_-)\, e^{i\Delta Kz} + \chi_{xy}(\omega = -\Omega+\omega_+) \times H_1(\Omega)\mathcal{E}_y(\omega_+)\, e^{-i\Delta Kz}], \quad (43b)$$

$$\frac{d}{dz}\mathcal{E}_y(\omega_-) = 2\pi ik\,[\chi_0(\omega_-)\mathcal{E}_y(\omega_-) + \chi_{yx}(\omega_- = -\Omega+\omega)\, H_1(\Omega)\mathcal{E}_x(\omega)\, e^{-i\Delta Kz}], \quad (43c)$$

where $\Delta K = K + k - k_+ = K - k + k_-$, and because we seek steady-state solutions, we have set the time derivatives to zero.

E. Phase Matching

One can show from (43) that for optimum coupling between the carrier wave and the upper sideband wave, it is necessary to fulfill the following phase-matching condition:

$$n_0'(\omega_+)\vec{k}_+ = n_0'(\omega)\vec{k} + \vec{K}, \quad (44)$$

where $n_0'(\omega_+)$ and $n_0'(\omega)$ are the real parts of the isotropic indices of refraction of the vapor at frequencies ω_+ and ω, respectively. We can write the real part of the isotropic index of refraction as

$$n_0'(\omega) \cong 1 + 2\pi\chi_0'(\omega), \quad (45)$$

where $\chi_0'(\omega)$ is the real part of the complex isotropic susceptibility defined by (27).

Similarly, one can show that for optimum coupling between the carrier wave and the lower-sideband wave, it is necessary to fulfill the following phase-matching condition:

$$n_0'(\omega_-)\vec{k}_- = n_0'(\omega)\vec{k} - \vec{K}. \quad (46)$$

The phase-matching conditions of (44) and (46) can be met by adjusting the guide wave vector $\vec{K}$ of the microwaves. The value of $\vec{K}$ required for proper phase matching can be written as

$$\vec{K} = \vec{K}_0 + \delta\vec{K}, \quad (47)$$

where $\vec{K}_0$ is the free-space wave vector of the microwaves ($K_0 = \Omega/c$). Therefore, to satisfy condition (44), the value of δK required can be written as

$$\delta K = 2\pi k\,[\chi_0'(\omega_+) - \chi_0'(\omega)], \quad (48)$$

and to satisfy (46), the value of δK required can be written as

$$\delta K = 2\pi k\,[\chi_0'(\omega) - \chi_0'(\omega_-)]. \quad (49)$$

From (48), (49), and the expression for the isotropic susceptibility given by (27), we note that the phase-matching conditions depend on the atomic density N, and the quantity $\langle\vec{I}\cdot\vec{J}\rangle$. The behavior $\chi_0'(\omega)$ as a function of optical frequency in the vicinity of the D_1 transition for the case without optical pumping and for the case with optical pumping is shown in Figs. 4(a) and 4(b), respectively. The atomic density assumed in Fig. 4 was estimated from published[22] rubidium-vapor-pressure data for a saturated vapor at 70 °C. The value of $\langle\vec{I}\cdot\vec{J}\rangle$ used in Fig. 4(b) was estimated to represent actual experimental conditions. One can see in Fig. 4 that because $\chi_0'(\omega)$ varies so rapidly with optical frequency, it would be difficult to select a combination of a carrier frequency, an upper-sideband frequency, and a lower-sideband frequency which would satisfy both (48) and (49) with the same value of δK.

The propagation equation (43) can be solved numerically by computer. In Fig. 6 we show the calculated modification of the spectral profile of Rb^{85} D_1 light which has passed through a 45-cm length of Rb^{87} vapor. The transmitted spectral profile was obtained by solving (43) for a range of carrier frequencies which spanned the spectral profile of Rb^{85} D_1 light. The vapor parameters (N and $\langle\vec{I}\cdot\vec{J}\rangle$) used in the calculation were assumed to represent the typical experimental conditions. The values of the frequency-response functions for

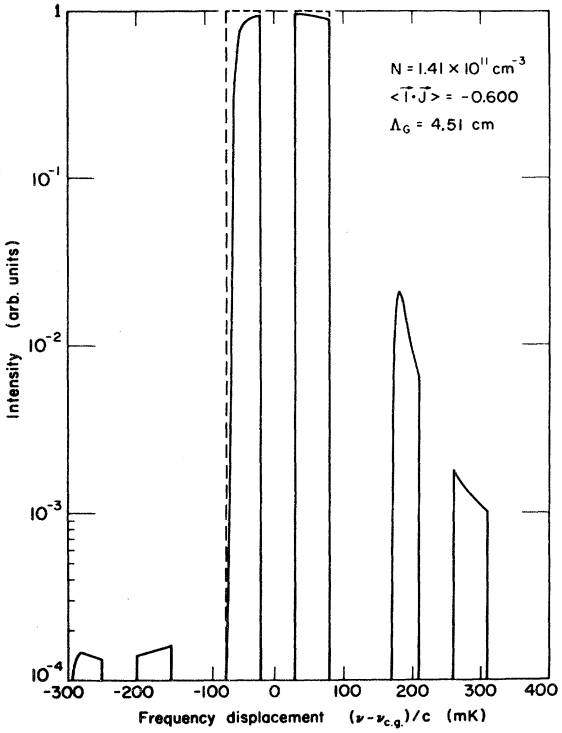

FIG. 6. Calculated spectral profile of carrier sidebands after carrier light has traversed 45 cm of Rb^{87} vapor. The initial spectral profile of the carrier light is represented by the broken line.

the Rb^{87} susceptibilities $\chi_0(\omega)$, $\alpha_{gt}(12;\omega)$, and $\alpha_{gt}(21;\omega)$ were taken from the curves shown in Figs. 4(b) and 5. The microwave frequency was taken to be on resonance ($\Omega = \omega_0 + \Delta\omega_t$) and the magnitude of the coherence, $|\sigma|$, was estimated from Fig. 2 to be $|\sigma| = 0.0325$. In Fig. 6, the initial profile of the Rb^{85} light (indicated by the broken line) was assumed for simplicity to be two rectangular-shaped lines designated as components *e* and *f* to represent the $F = 3$ and $F = 2$ hfs components, respectively. In the calculation we have taken the value of the guide wavelength of the microwaves to be $\Lambda_G = 4.51$ cm such that the phase-matching condition of (49) is satisfied to give perfect phase matching between a carrier at -40 mK and an upper sideband as 188 mK (the microwave frequency being 288 mK). The spectral profile of the transmitted light is represented by the solid curve in Fig. 6. We note that the components of the carrier light have been partially attenuated because of the overlap with the Rb^{87} absorption line. But in addition, sideband components designated by *a*, *b*, *c*, and *d* which were not present in the initial spectral profile have appeared. The strongest sideband component is the one which peaks at 188 mK, because we had chosen to precisely phase match the optical wave at 188 mK with an optical wave at -40 mK. Other sideband components which are not so well phase matched are also present but are much weaker. Needless to say, the spectral profile of the sidebands depends on which waves one has phase matched. In designing an experiment to observe the sidebands, one needs to first decide which waves one wishes to phase match and then to adjust the guide wave vector of the microwaves to the proper value as determined by the conditions (48)–(50). However, to apply these conditions, one needs to know precisely the values of certain vapor parameters such as the atomic density N and the hfs polarization $\langle \vec{I} \cdot \vec{J} \rangle$. Unfortunately, these quantities are very difficult to determine accurately; furthermore, they tend to be rather inhomogeneous throughout the resonance cell. Therefore, in practice one is not always able to predict precisely the spectral profile of the sidebands.

III. EXPERIMENT

A. Experimental Procedure

A schematic diagram of the experimental apparatus is shown in Fig. 7. A 45-cm-long cylindrical resonance cell filled with a small amount of Rb^{87} metal and 12 torr of nitrogen buffer gas was placed inside of a microwave cavity which was tuned to resonate at 6.835 GHz in the TE_{01n} mode. The cavity and cell were situated within three pairs of mutually orthogonal Helmholtz coils which served to cancel out the earth's magnetic field and to provide a static 2-G magnetic field along the z direction. The resonance cell was optically pumped by resonance light from a long Rb^{85} lamp, which was located parallel to the cavity axis. The Rb^{87} atoms in the resonance cell are pumped from the $F = 2$ hfs level into the $F = 1$ hfs level of the ground state. Microwaves from a stabilized klystron were introduced in the cavity to drive the 0-0 hfs transition in the Rb^{87} atoms, thus producing coherence in the vapor. The microwaves were square-wave modulated to permit the accompanying changes in the sideband intensity to be detected by phase-sensitive detection.

The optical carrier light was provided by a second Rb^{85} lamp which was situated at one end of the cavity. A linear polarizer P_1 polarized the carrier light before it enters the cavity. The transmitted light emerging from the cavity passed through another polarizer P_2, which was orthogonal to P_1. The two linear polarizers P_1 and P_2 served to filter out the carrier light while passing the sideband light. Finally, the transmitted light beam was frequency analyzed with a scanning Fabry-Perot interferometer for which a Rb D_1-interference filter was used as a preselector. The optical detector used with the interferometer was a refrigerated

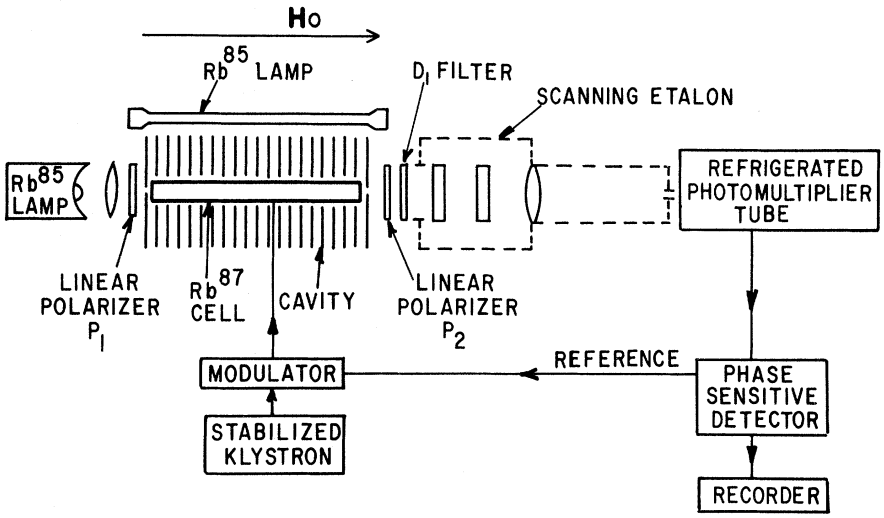

FIG. 7. Experimental apparatus.

photomultiplier tube. The photomultiplier signal was detected with a phase-sensitive detector in synchronism with the modulation of the microwaves

B. Apparatus

1. Microwave Cavity

The microwave cavity (see Fig. 8) is made from a number of $5\times5\times\frac{1}{16}$-in. brass plates, each having a circular hole in its center. The plates were arranged in a structure which kept them 1 cm apart with the holes aligned. One end of the cavity was terminated by a plate with a smaller hole while the other end had a 10-cm-long section of ordinary circular waveguide terminated by a perforated shorting plug. This type of cavity will only contain axially symmetric TE modes and the cavity used in this experiment was designed to operate in the TE_{01n} mode. The unloaded Q of the cavity without the resonance cell was on the order of 10^4.

The resonance cell, which was situated coaxially inside the cavity was supported by annular spacers made from Ecco foam.[23] Placing the quartz cell in the cavity reduced the Q substantially. This may have been due to either imperfect alignment of the axis of the cell with the axis of the cavity or due to an aximuthal nonuniformity in the wall thickness of the quartz tube. A nonaxially symmetric distribution of quartz in this cavity would result in mixing of the TE_{01n} modes with nonaxially symmetric modes which are very lossy. The Q of the cavity with the resonance cell in place was on the order of 100.

In order to satisfy the phase-matching conditions given by (44) or (46), the guide wave vector in the cavity must be adjusted to the proper value determined by (48) and (49): The guide wave vector in the cavity can be adjusted by varying the transverse

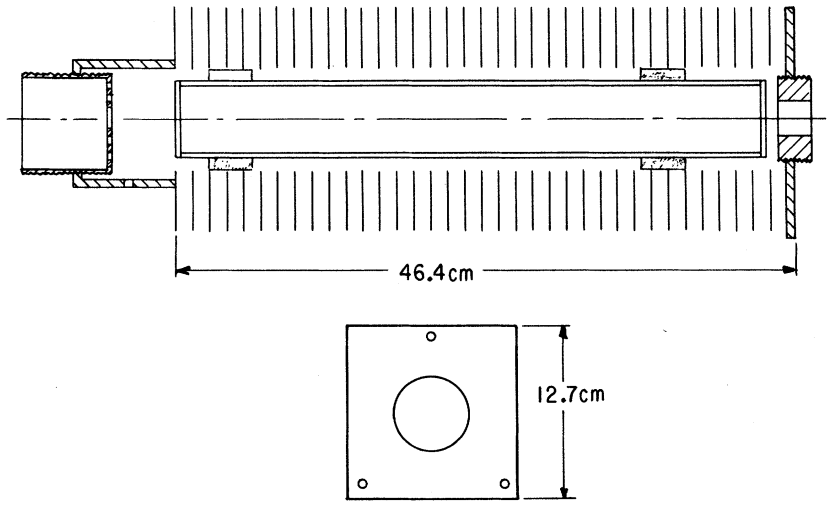

FIG. 8. Microwave cavity.

dimensions of the cavity; however, one must take into account the loading effects of the quartz resonance cell. The quartz, which has a relatively high dielectric constant will tend to lengthen the guide wave vector. Given the inner and outer radii of the quartz resonance cell, one can usually solve for the cavity radius which would give a particular value for the guide wave vector. In a cavity like the one shown in Fig. 8, the fields penetrate a small distance between the plates so that the effective radius of the cavity is somewhat larger than the radius of the holes in the plates. Therefore, the holes of the plates must be cut with their radii smaller than the required cavity radius by an amount equal to the penetration depth of the fields. The penetration depth was determined by measuring the guide wave vector of the cavity without the cell, and relating the measured value to an effective radius of the cavity.

The advantages of the cavity shown in Fig. 8 were the following: Large areas of the resonance cell inside the cavity were made accessible to pumping light from a lamp which was outside the cavity. The resonance cell could be illuminated uniformaly by the pumping light along its entire length. This latter advantage was particularly important in that it made phase-matching possible and also reduced the inhomogeneous broadening of the microwave resonance due to light shifts.[24]

2. *Resonance Cell*

The resonance cell was made from fused-quartz tubing (see Fig. 9). The quartz tubing was first etched in a 20% solution of HF to remove the graphite film that is usually found on the walls of commercial quartz tubing. The cell was then constructed and sealed onto a vacuum system where it was baked at 500 °C for 24 hours while a pressure of 2×10^{-7} torr was maintained. After the cell was allowed to cool, 99.2% isotopically pure Rb^{87} metal was distilled into one of the reservoirs. Care was taken not to allow the rubidium metal to condense in the cell proper as this would increase the microwave loss when the cell is placed inside the cavity. Nitrogen gas at a pressure of 12 torr was also introduced into the cell to serve both as a buffer gas and also as a quenching gas for fluorescently scattered radiation.[25] After sealing off the cell, we found that there was a sharp gradient in the rubidium-vapor density along the length of the cell away from the reservior. This was probably due to some sort of chemical reaction taking place between the rubidium vapor and the quartz walls. Such reactions have been reported by other workers.[26] This problem was particularly severe in our case because of the long cylindrical geometry of our cells. However, the gradient was found to diminish with time and disappeared entirely after about two months. This "aging" period for the cells was later reduced considerably by first coating the cell walls with Paraflint,[27] which seemed to be less reactive with rubidium. Then rubidium was distilled into the cell reservoir and the cell was sealed off without buffer gas. With no buffer gas to hinder the diffusion of the rubidium atoms, the cell walls saturated in about one week. Buffer gas was added to the cell via a break-off seal after the gradients had disappeared.

3. *Resonance Lamps*

The Rb^{85} lamp which was used for optical pumping of the Rb^{87} vapor is shown in Fig. 10. The lamp consisted of a Pyrex dc discharge tube containing Rb^{85} separated isotope and 2 torr of Krypton gas. The lamp electrodes were made from self-heating oxide-coated filaments which were capable of sustaining the discharge at currents of as high as 2 A. An evacuated jacket surrounded most of the active region of the discharge to keep that region hot. The Rb^{85} resonance light from this lamp was focused onto the resonance cell by an elliptical reflector.

The lamp which provided the carrier light was a commercially available Varian X49-609 spectral lamp containing Rb^{85} separated isotope and about 2 torr of krypton gas.

4. *Interferometer*

The Fabry-Perot interferometer was a C. D. Grant model FP-1. The instrument was scanned

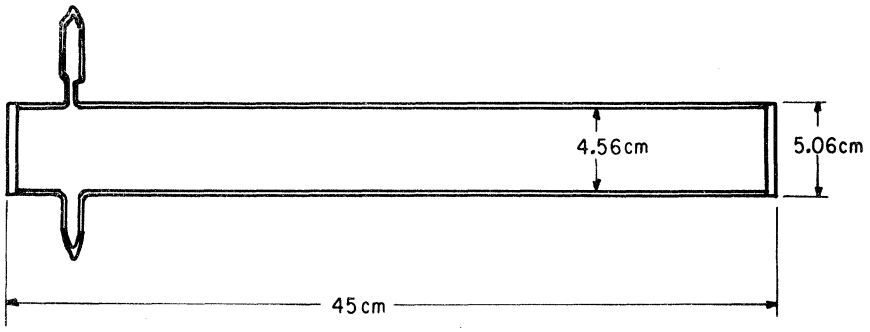

FIG. 9. Resonance cell.

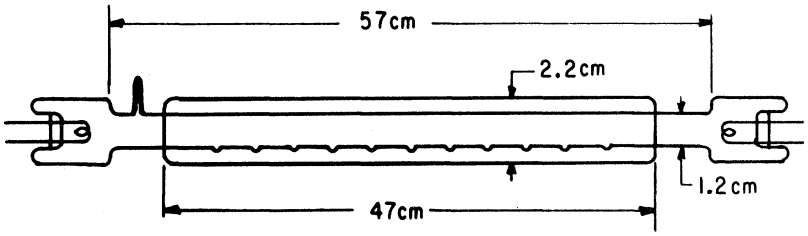

FIG. 10. Rb^{85} resonance lamp used for optical pumping.

by applying a ramp voltage to three stacks of piezoelectric disks which translated one of the two plane parallel plates. The 2-in. -diam plates were obtained from the Perkin–Elmer Corp. The manufacturer claimed the flatness of the plates to be $\lambda/200$. The reflectance of the dielectric coatings on the plates was 97% at the D_1 and D_2 lines of rubidium. The central fringe of the interference pattern was imaged onto a 500-μm pinhole by a 300-mm-focal-length lens. As the plate spacing was scanned, the change in intensity of the central fringe was recorded by a photomultiplier tube located directly after the pinhole.

A plate spacing of 0.5 cm was used which gave a free spectral range of 1000 mK. A narrow-band interference filter (from Baird Atomic) which had a passband of 90 Å centered at 7948 Å and a peak transmittance of 52% was used as a preselector for the interferometer. The finesse of the interferometer, which is the ratio of the free spectral range to the instrumental width, was estimated to be 35 at 7947 Å.

5. *Microwaves*

A schematic of the apparatus used to provide the microwaves is shown in Fig. 11. The microwaves were generated by a Varian X-26B reflex klystron which was stabilized by a Frequency Engineering Laboratories A130K frequency synchronizer. The synchronizer phase locks the klystron

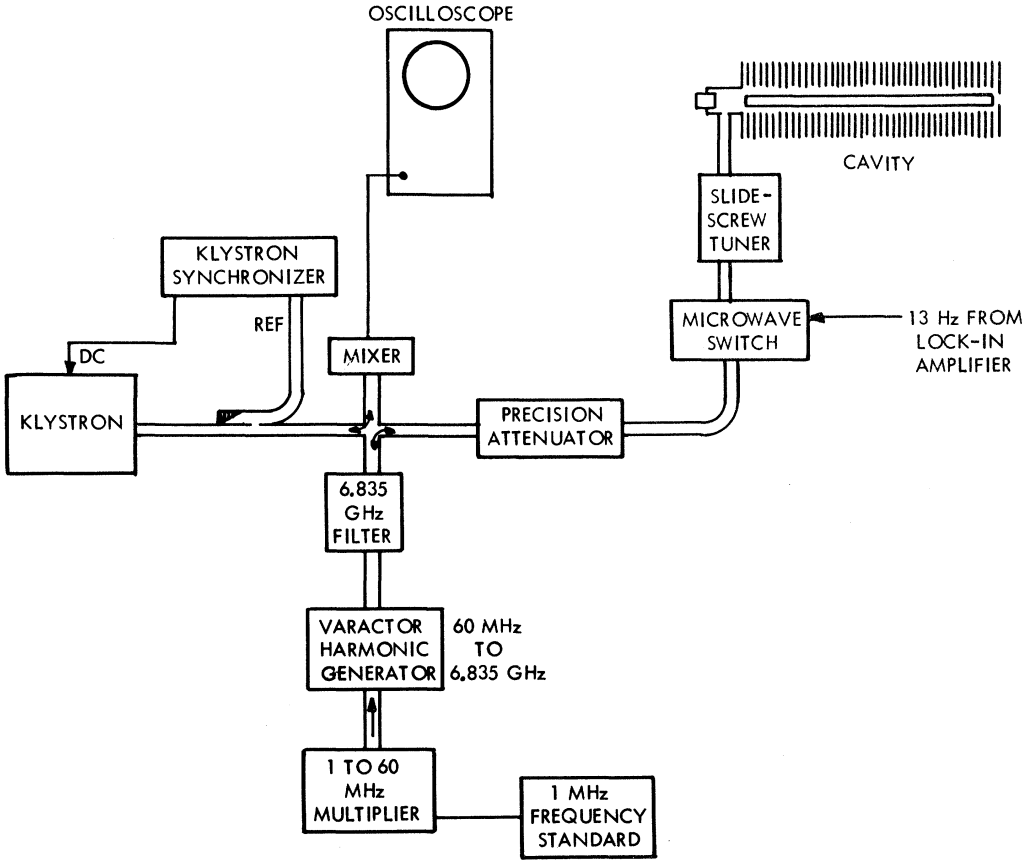

FIG. 11. Schematic diagram of circuit used to provide stabilized microwaves.

frequency to that of an oven-controlled quartz crystal oscillator; thus the short term stability of the microwave frequency was kept stable to better than one part in 10^8. Frequency stability of this order was necessary as the width of the microwave resonance was on the order of 1 kHz. As a check on the long-term stability of the klystron, the microwave frequency was compared with 6835th harmonic of a 1-MHz NBS quartz frequency standard. The microwaves from the klystron first passed through an FXR C164A precision attenuator and were then chopped by a Hewlett-Packard 33053-A microwave switch which was actuated by a 13-Hz reference signal from a lock-in amplifier. The microwaves were fed to the cavity through a slide-screw tuner. Despite the low Q of the cavity when the resonance cell was inside, the klystron had more than enough power to drive the microwave transition. The power required to saturate the microwave transition is only on the order of 10^{-5} W.

6. Detection

The photomultiplier was an EMI 9658RA which had an extended-red-response version of the S-20 photosurface. The quantum efficiency was claimed by the manufacturer to be 5% at 7947 Å. To reduce the dark current, the tube was cooled to -30 °C in a thermoelectric refrigerator housing, and was used with a magnetic lense before the photocathode. Operated in this way, the tube's dark current was less than 0.1 nA. The output of the photomultiplier went directly to a Princeton Applied Research HR-8 lock-in amplifier.

The linear polarizers P_1 and P_2 were Polaroid HN-38 sheet polarizers. The transmission for 7947 Å light was 39% when P_1 and P_2 were parallel but only 0.2% when they were crossed.

C. Experimental Results

1. Observations with the Fabry-Perot Interferometer

The data recorded with the apparatus of Fig. 7 is shown in Fig. 12. Figure 12(a) shows the spectral profile of the transmitted light from the cavity observed with the polarizers P_1 and P_2 crossed; hence the carrier-light components have been mostly removed. This signal was recorded with 30-msec time constant on the lock-in amplifier, and the duration of the interferometer scan was 1 min. Figure 12(b) shows the spectral profile of the transmitted Rb^{85} carrier light (observed with P_1 and P_2 parallel). The initial spectral profile of the carrier light before it enters the cavity is shown in Fig. 12(c). For comparison, the spectral profile of Rb^{87} D_1 light is shown in Fig. 12(d). We note in Fig. 12(a) that four components (designated by *a*, *b*, *c*, and *d*) are clearly resolved. On comparing Fig. 12(a) with Fig. 12(c) we also not that components *a* and *b* of Fig. 12(a) are displaced 228 mK (228 mK≈ 6.8 GHz) to the low-frequency side of components *e* and *f* of Fig. 12(c), respectively. Also, components *c* and *d* of Fig. 12(a) are displaced 228 mK to the high-frequency side of components *e* and *f* of Fig. 12(c), respectively. Furthermore, the spectral components of Fig. 12(a) were not due to fluorescently scattered pumping light as they do not coincide with the spectral components of Rb^{87} resonance light [Fig. 12(d)] and they also disappeared when the carrier light was removed as shown in Fig. 12(e). The components remaining in Fig. 12(e) were due to the small amount of carrier light which is transmitted even when P_1 and P_2 were crossed. Since the absorption of the overlapping component of Rb^{85} light by the vapor is increased when the microwaves are on, the transmitted carrier light is modulated at the chopping frequency of the microwaves and was,

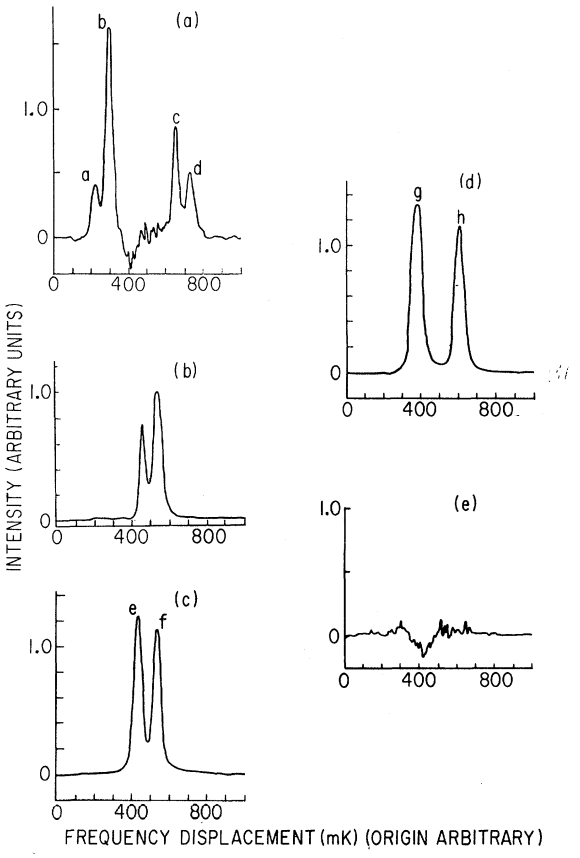

FIG. 12. (a) Spectral profile observed with the lock-in detection when the polarizers P_1 and P_2 were crossed. (b) Spectral profile observed when the polarizers P_1 and P_2 were parallel. (c) Spectral profile of Rb^{85} D_1 light (carrier light). (d) Spectral profile of Rb^{87} D_1 light. (e) Spectral profile observed with lock-in detection with polarizers P_1 and P_2 crossed when the carrier light was removed.

therefore, detected by the lock-in amplifier.

We therefore conclude that the spectral components seen in Fig. 12(a) are upper and lower sidebands which have been generated onto the spectral profile of Rb^{85} resonance light by the microwave coherence in the Rb^{87} vapor. The intensity of the most intense sideband component was about 1.3% of the intensity of its corresponding carrier component.

The sideband signals were detected with sufficiently high signal-to-noise ratio to allow observation of the sideband without lock-in detection. Figure 13 shows the result when the output of the photomultiplier was connected directly to an oscilloscope. Here, the microwaves were not chopped, and the horizontal sweep of the oscilloscope was synchronized with the interferometer scan. The full horizontal sweep corresponds to 1000 mK.

Figure 13(a) shows the spectral profile observed when the polarizers P_1 and P_2 were parallel; i.e., only the transmitted carrier light passed P_2. The spectral profile observed when P_1 and P_2 were crossed is shown in Fig. 13(b). The sideband components *a*, *b*, *c*, and *d* are indicated in this figure. Also present in Fig. 13(b), were the components *e* and *f* or Rb^{85} light from the pumping lamp which was scattered by the cavity plates and the resonance cell walls. Figure 13(c) shows the spectral profile observed when the carrier lamp was removed. One can see in this figure that in addition to components *e* and *f*, there were also present the small components *g* and *h* which were due to the fluorescently scattered Rb^{87} light from the vapor. The Rb^{87} fluorescence had been greatly reduced by the presence of the nitrogen gas in the cell. Figure 13(d) shows the spectral profile which was observed when the carrier lamp was replaced but the microwave frequency was tuned off resonance. We see that the sideband components were present only when the microwave frequency was on resonance.

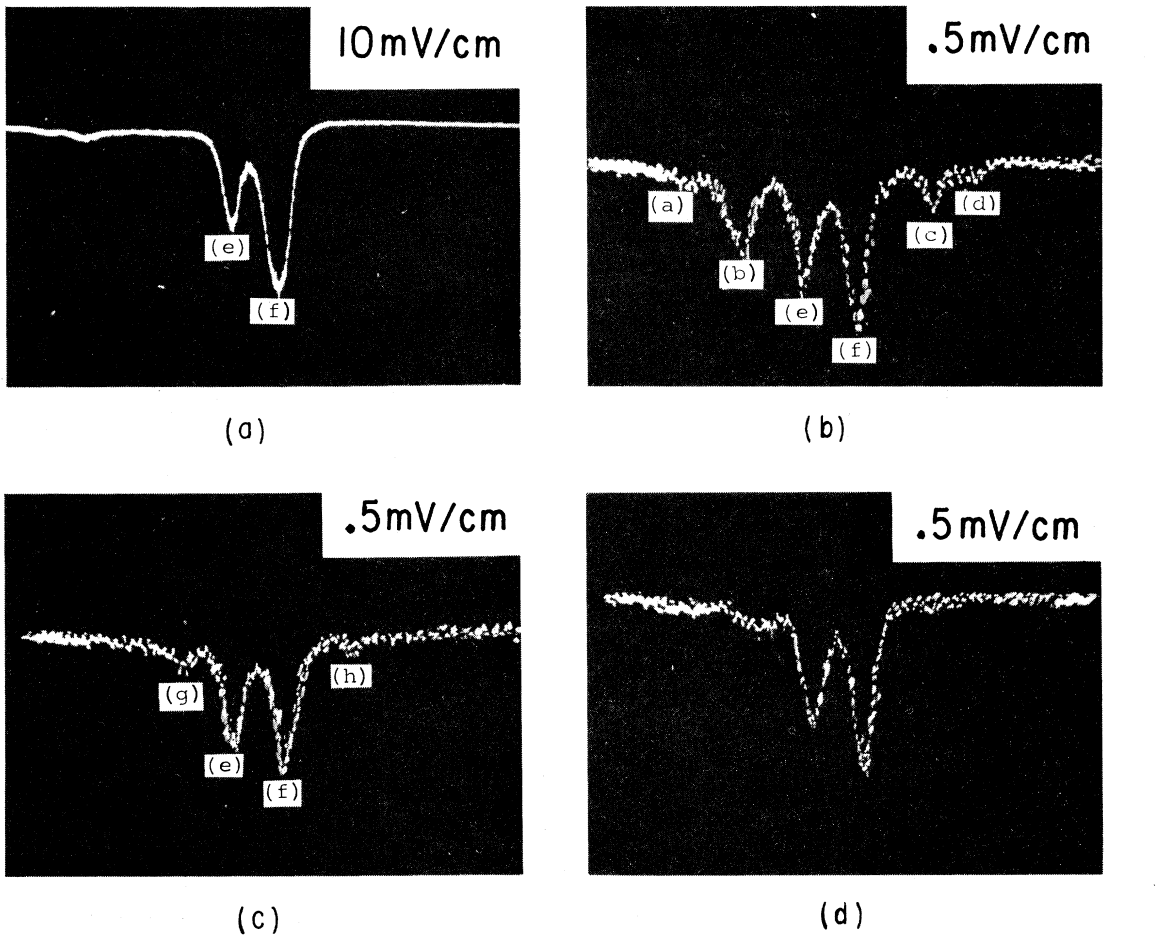

FIG. 13. (a) Oscillogram of the photomultiplier output when the polarizers P_1 and P_2 were parallel. (b) Oscillogram of the photomultiplier output when the polarizers P_1 and P_2 were crossed. (c) Oscillogram of the photomultiplier output when the polarizers P_1 and P_2 were crossed but the carrier light was removed. (d) Oscillogram of the photomultiplier output when the polarizers P_1 and P_2 were crossed but the microwave frequency was off resonance.

2. Observations without the Interferometer

The following data were recorded with the interferometer removed; i.e., the photomultiplier was situated immediately after the polarizer P_2. The polarizers P_1 and P_2 were crossed so that the signals represent the integrated intensity of all the spectral components of Fig. 12(a). Figure 14 shows the integrated intensity of the sidebands as a function of microwave frequency. The microwave frequency was swept over a range of 20 kHz about the hfs resonance frequency. The sideband intensity versus microwave-frequency signal obtained for low microwave power is shown in Fig. 14(a) while Fig. 14(b) shows the same signal obtained for high microwave power. We observed in Fig. 14(a) that for low microwave power, the sideband intensity as a function of microwave frequency obeyed a normal resonance shape. However, in Fig. 14(b), we observe that for high microwave power, the intensity of the sidebands at the center of the resonance had decreased. This is what one would expect since the sideband intensity is approximately proportional to the square of the coherence ($|\rho_{37}|^2$) for small values of coherence. We have already shown [see Fig. 3(b)] that when the hfs transition is saturated, the magnitude of the coherence decreases at the center of the hfs resonance.

In Fig. 15 we have plotted the integrated intensity of the sidebands versus the magnitude of the microwave magnetic field, H_1, while the microwave frequency was kept on the center of the resonance. We see that the sideband intensity attained a maximum for a field strength of about 1.0×10^{-4} G, and decreased for greater or lesser field strengths. Upon comparing Fig. 15 with Fig. 2, we note that the sidebands of Fig. 12(a) have the same qualitative dependence on the microwave field strength as does the coherence $|\rho_{37}|$. The functional dependence of the sideband intensities on the coherence is quite complicated for long lengths of vapor but one can obtain it by solving the propagation equations of (43).

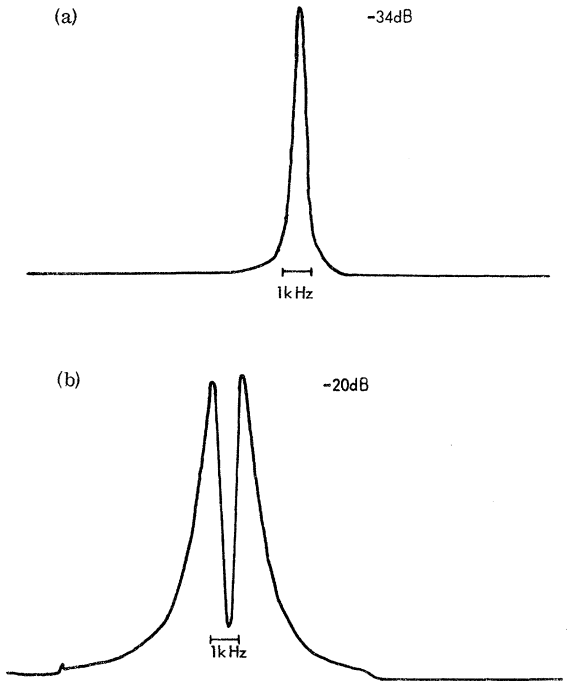

FIG. 14. (a) Integrated sideband intensity vs microwave frequency for low microwave power. (b) Integrated sideband intensity vs microwave frequency for high microwave power.

3. Studies of Phase Matching

One can show by solving (43) that the intensity of a sideband wave which is perfectly phase matched with its carrier wave will increase monotonically with the length of the cell until the power in the carrier wave is depleted. On the other hand, the intensity of an imperfectly phase-matched sideband wave will reach a maximum before the carrier power is depleted and then will decrease. The interaction length l for a particular monochromatic sideband wave is that distance of propagation at which the sideband intensity reaches its first maximum before the carrier is depleted.

A study was made of the growth of the sidebands as a function of the active length of the cell. The latter quantity was varied by blocking off segments of the resonance cell length from the pumping light, beginning from the end away from the carrier lamp. Then in the unilluminated regions of the cell, the coherence vanished and no conversion takes place. Since the sidebands do not overlap the Rb^{87} absorption lines, they propagate through the inactive region of the cell unattenuated. The effects of varying the active length of the cell on the sidebands are shown in Fig. 16. We can see that all the resolvable sideband components grew monotonically with increasing cell length, although they do not all grow at the same rate. It appeared that the upper sideband components grew faster initially than the lower sideband components, but the latter eventually caught up with and exceeded the former.

Figure 17(a) shows the dependence of the integrated sideband intensity on the active cell length. In this case, the average guide wavelength of the microwaves was 4.5 cm. We note that for each of the cell temperatures shown in Fig. 17(a), the integrated sideband intensity grew monotonically with active cell length with the rate of the growth increasing with the cell temperature. However, for cell temperatures higher than 70 °C, the rate of growth decreased with temperature, but in addition, a small oscillation appeared superimposed on the otherwise monotonic growth of the integrated side-

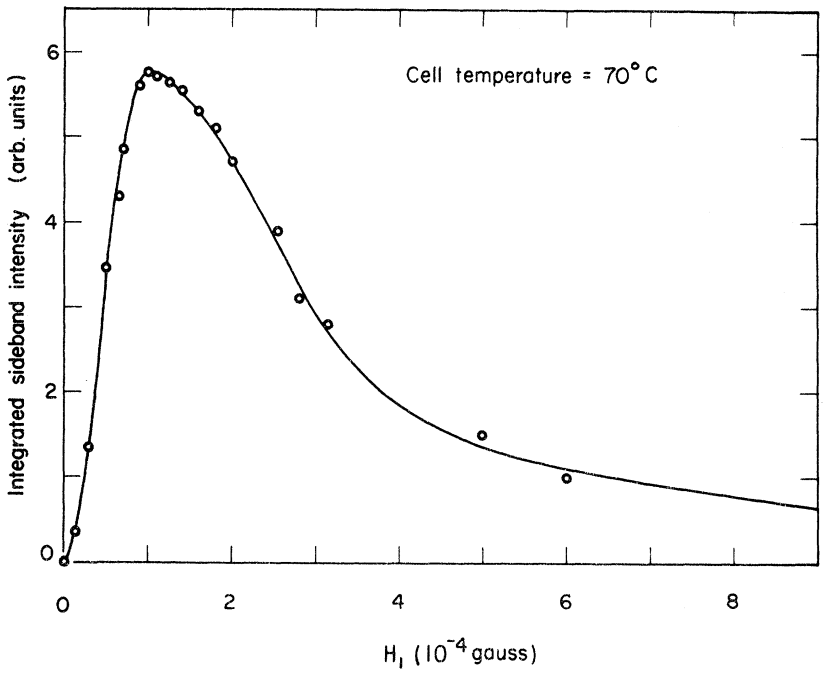

FIG. 15. Integrated sideband intensity vs the magnitude of the microwave field H_1.

band intensity, as shown in Fig. 17(b). The period of the oscillation was observed to be equal to half the guide wavelength of the microwaves. Also, the minima of the oscillation coincided with the positions of the nodes of the cavity fields. This behavior of the sidebands had not been predicted by our theory because we had only considered the interaction of the carrier light with the component of microwave field in the cavity which is traveling in the same direction as the carrier [see (41)], i.e., the forward wave interaction. However, it is also possible to have a backward wave interaction in which the carrier light interacts with the component of microwave field which is traveling in the opposite direction. We had assumed in Sec. II that the backward wave interactions were badly phase matched and could, therefore, be neglected. If, however, sideband waves were being simultaneously generated by both forward and backward wave interactions, then the sideband wave which is generated by the forward wave interaction would interfere with the sideband wave of the same frequency generated by the backward wave interaction. One can show this by using the propagation equations (43) to account for the forward wave interactions. A similar set of propagation equations to account for the backward wave interactions can be obtained by taking the microwave magnetic field to be of the form

$$\vec{H}(z,t,\Omega) = -\vec{H}_1(\Omega)\, e^{i(-Kz-\Omega t)} + \text{c.c.}, \qquad (50)$$

and incorporating it into the polarizations of (42).

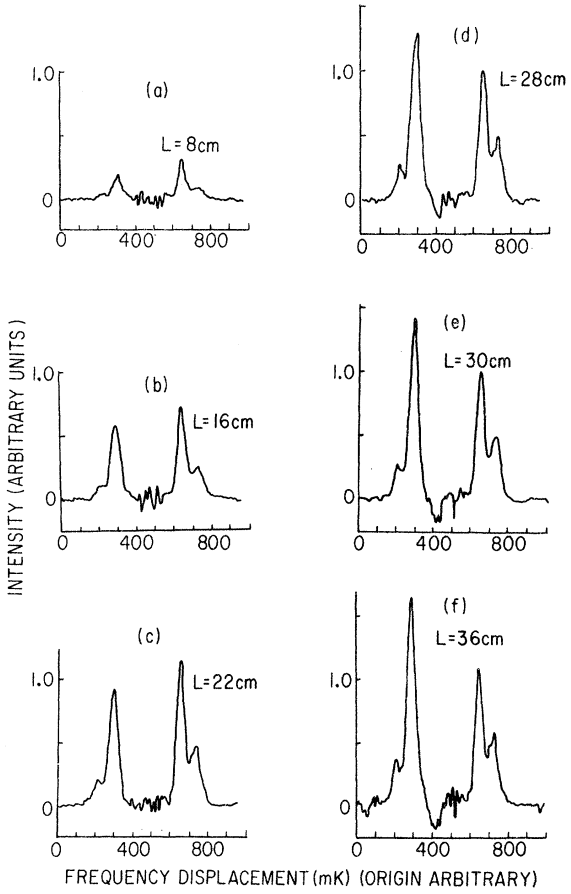

FIG. 16. Sideband spectral profile vs active cell length.

The polarizations are then substituted, as before, into the first-order wave equation of (40). The total sideband field then is the superposition of the solutions of (43) and those of the counterpart of (43) for backward wave interactions. Suppose a sideband wave of frequency ω_+ is composed of components due to both forward and backward wave interactions, but neither component is well phase matched. Figure 18(a) shows the wave-vector diagram representing the generation of an upper sideband of frequency ω_+ and wave vector $n'(\omega_+)\vec{k}_+$ due to the forward wave interaction of a carrier wave of wave vector $n'(\omega)\vec{k}$ and a microwave field of wave vector $\vec{K}$. Figure 18(b) shows the wave-vector diagram representing the generation of an upper-sideband wave of the same frequency but due to the backward wave interaction of the same carrier wave and an oppositely directed microwave field. The quantities ΔK_1 and ΔK_2 in Fig. 18 give the extent of the phase mismatch for the forward and the backward wave interactions. One can show by obtaining the first-order solutions to Eq. (43) and its counterpart for backward wave interactions that the amplitudes of the sideband components which are imperfectly phase matched will vary sinusoidally with the distance of propagation. We can, therefore, write the amplitude of the sideband wave at frequency ω_+ to first order as

$$\mathcal{E}(\omega_+) = A\sin(\Delta K_1 z) - B\sin(\Delta K_2 z), \tag{51}$$

where A is the maximum amplitude of the component arising from the forward wave interaction and B is the maximum amplitude of the component arising from the backward wave interaction. Equation (51) can be rewritten to give

$$\mathcal{E}(\omega_+) = (A - B)\sin(\Delta K_1 z) + 2B\cos[n'(\omega_+)k_+ - n'(\omega)k]\, z \sin Kz, \tag{52}$$

where we have used the relations taken from Fig. 18 that

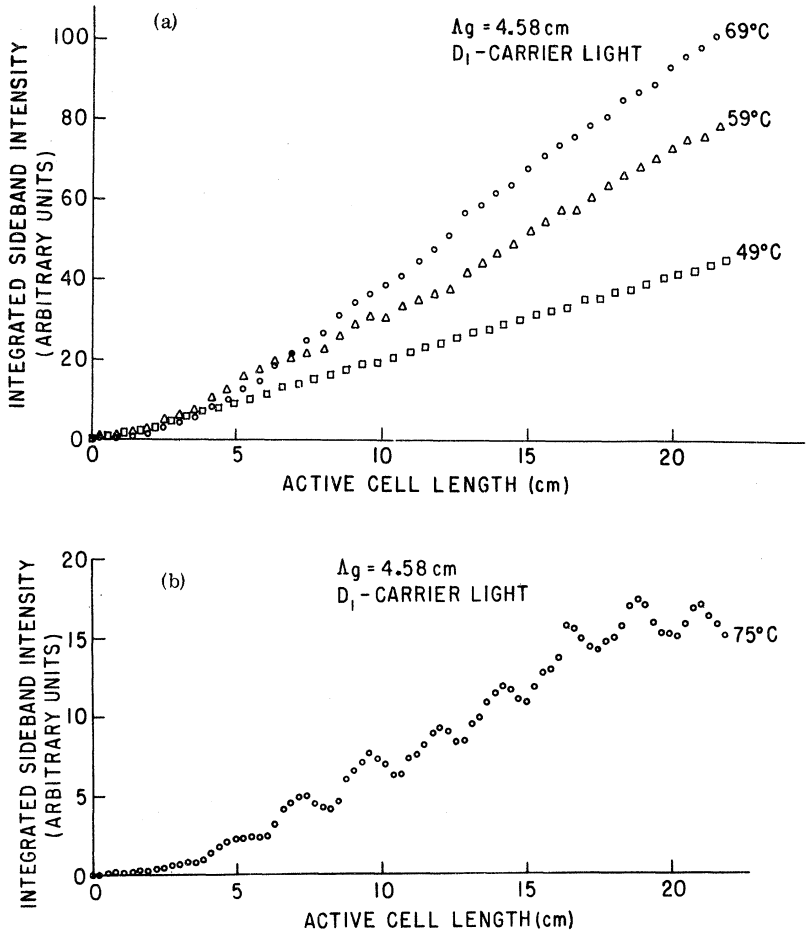

FIG. 17. (a) Integrated sideband intensity vs active cell length at three different cell temperatures each showing a monotomic increase of the sideband intensity with cell length. (b) Integrated sideband intensity versus active cell length showing oscillatory behavior of the sideband intensity with cell length.

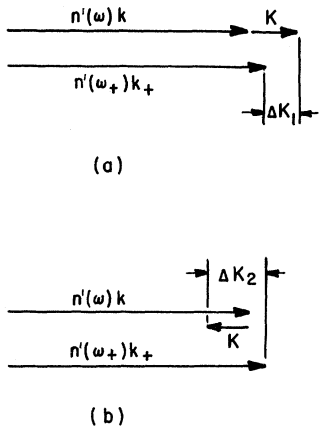

FIG. 18. (a) Wave-vector diagram representing imperfectly phase-matched forward-wave interaction (not drawn to scale). (b) Wave-vector diagram representing imperfectly phase-matched backward wave interaction (not drawn to scale).

$$\Delta K_1 = n'(\omega_+)k_+ - n'(\omega)k - K$$

and

$$\Delta K_2 = n'(\omega_+)k_+ - n'(\omega)k + K.$$

We can see from (52) that the sideband-wave amplitude will have a minimum when $\sin Kz$ is zero. Furthermore, these minima occur at the same positions along the length of the cavity as do the nodes of the microwave field. One can show that the same effect takes place for lower-sideband waves.

In order to further demonstrate the relationship between the phases of the sideband waves and the phase of the microwave fields in the cavity, we rearranged our apparatus as shown in Fig. 19. Here we reflect the transmitted light from the cavity back into the cavity by means of a spherical mirror. The mirror holder was mounted on tracks so that it could be translated parallel to the axis of the cavity. The reflected light, after it had passed through the cavity, was detected at the end near the carrier lamp. A dielectric coated beam splitter was used to direct the light through a linear polarizer P_2 and a D_1 filter, and into a photomultiplier tube. The polarizers P_1 and P_2 were crossed to eliminate the carrier light. The integrated sideband intensity was recorded as the mirror was scanned in one direction. What was observed was a set of interference fringes (see bottom of Fig. 19) with the fringe spacing being equal to half the free-space wavelength of the microwaves.

These fringes can be understood quantitatively with the aid of the propagation equations (43). However, a qualitative understanding of the effect shown in Fig. 19 can be gotten by considering the following. Suppose the wave front of the optical carrier wave enters the cavity from the left at time t. Inside the cavity there is a microwave field traveling to the right,

$$H_1(\Omega)\, e^{i(Kz-\Omega t)} + \text{c. c.}, \tag{53}$$

and a microwave field traveling to the left

$$-H_1(\Omega)\, e^{i(-Kz-\Omega t)} + \text{c. c.} \tag{54}$$

Assuming that only forward wave interaction takes

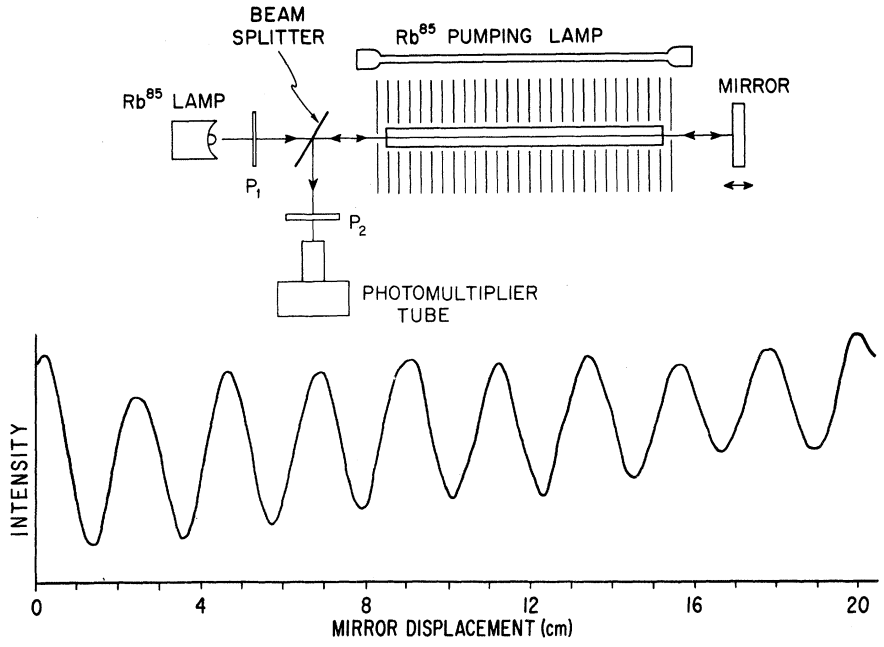

FIG. 19. Apparatus used to demonstrate interference of sidebands. The lower portion of this figure shows the intensity detected by the photomultiplier tube as the mirror spacing was scanned.

place, the carrier wave as it propagates to the right interacts with the right-running microwave field, generating sideband waves. The time of arrival of the carrier wave front at the right end of the cavity is $t+L/n'(\omega)c$, where L is the length of the cavity. Thus, as the carrier wave front leaves the cavity, the phase of the right running microwave field is $KL-\Omega[t+L/n'(\omega)c]$. After leaving the cavity, the carrier wave, along with the sideband waves which were generated in the first pass, propagates a distance d through free space towards the mirror which reflects these waves back toward the right end of the cavity. The time of arrival of the wave front back at the right end of the cavity is $t+L/n'(\omega)c+2d/c$. The carrier wave which now propagates to the left will interact only with the left-running microwave field. The phase of the left-running microwave field as the carrier wave front reenters the cavity from the right is

$$\pi+\{-KL-\Omega[t+L/n'(\omega)c+2d/c]\}. \tag{55}$$

In order for the sideband waves which are generated during the second pass of the carrier wave to be in phase with the sideband waves which were generated during the first pass, the phase of the left-running microwave field, as the carrier wave front reenters the cavity, must be the same as that of the right-running microwave field when the carrier wave left the cavity. This condition may be written as

$$\{KL-\Omega[t+L/n'(\omega)c]\} = \pi+\{-KL-\Omega[t+L/n'(\omega)c+2d/c]\}\pm n(2\pi), \quad n=\text{integer}. \tag{56}$$

Solving for d in (55) we obtain

$$d=\pm n\Lambda_0/2-(\text{const}), \tag{57}$$

where Λ_0 is the free-space wavelength of the microwaves. Therefore, from (57) we see that the separation of successive maxima of the sideband intensity corresponds to a translation of the mirror through a distance of $\Lambda_0/2$.

IV. CONCLUSIONS

We have directly observed the sidebands which were generated onto the spectral profile of an incoherent optical carrier by an alkali-metal-atom vapor with ground-state hfs coherence. This effect had been predicted by the semiclassical theory which we presented in Sec. II. We have not yet attempted to make any quantitative comparisons between our theory and our experimental results, because to make such comparisons, we would need to have accurate values for the various parameters of the alkali vapors. In particular, we would need to know the atomic density N and the degree of ground-state hfs polarization $\langle\vec{I}\cdot\vec{J}\rangle$, to an accuracy of a few percent. This is because the spectral profile of the sidebands is very sensitive to how one has phase matched the interacting waves, and the phase-matching conditions are primarily determined by N and $\langle\vec{I}\cdot\vec{J}\rangle$ [see (47)–(49)]. Although several methods are known for measuring N,[28] and for measuring $\langle\vec{I}\cdot\vec{J}\rangle$,[29] none of these methods would give measurements of the required accuracy.

However, we were able to make several qualitative comparisons between the theory and the experiment. The dependence of the sideband intensities on the microwave field shown in Figs. 14 and 15 clearly demonstrates the relationship between the sidebands and the microwave coherence in the vapor. The data shown in Figs. 16 and 17 demonstrate the sensitive dependence of the sideband conversion efficiency on the phase matching. Finally, the interference fringes shown in Fig. 19 demonstrate that the phases of the sidebands is determined by either the sum or difference of the phases of the carrier wave and the phase of the microwave field. Therefore, our observations seem to be in excellent qualitative agreement with our theory.

ACKNOWLEDGMENT

The author is indebted to Professor W. Happer for suggesting this experiment, and for advice and encouragement throughout the course of this work.

APPENDIX A: EVALUATION OF $\langle\vec{J}(F,F')\rangle$ FOR Rb^{87} GROUND STATE

The ground-state density matrix ρ can be written as

$$\rho=\sum_{F,F',m,m'}|F'm\rangle\langle Fm|\rho|F'm'\rangle\langle F'm'|. \tag{A1}$$

The expectation value of the operator $\vec{J}(11)$ is

$$\langle J(11)\rangle=\mathrm{Tr}[\rho\vec{J}(11)]=\sum_{Fm}\langle Fm|\rho\vec{J}(11)|Fm\rangle = \sum_{mm'}\langle 1m|\rho|1m'\rangle\langle 1m'|\vec{J}(11)|1m\rangle. \tag{A2}$$

We assume there are no coherences or population imbalances between the Zeeman sublevels within the $F=1$ hfs level so that

$$\langle 1m|\rho|1m'\rangle=0 \quad \text{for } m\neq m', \tag{A3}$$

and all the diagonal density matrix elements $\langle 1m|\rho|1m\rangle$ are equal. Hence (A2) can be written as

$$\langle\vec{J}(11)\rangle=\langle 11|\rho|11\rangle\sum_m\langle 1m|J_z|1m\rangle\hat{e}_z, \tag{A4}$$

where we have expanded the angular-momentum

operator $\vec{J}$ into its components

$$\vec{J}=\vec{J}_z\hat{e}_z-J_{+1}\hat{e}_{+1}-J_{-1}\hat{e}_{-1}. \tag{A5}$$

We can evaluate the matrix elements of J_z using the Wigner–Eckart theorem to give

$$\langle IJ1m|J_z|IJ1m\rangle=(-1)^{I-J}C(111;m\ 0\ m)[(2J+1)3]^{1/2}\times W(J1J2;I1)[(J(J+1)]^{1/2}. \tag{A6}$$

Substituting (A6) in (A4) and using the properties of the Clebsch-Gordan coefficients that

$$C(111;m\ 0\ m)=-C(111;-m\ 0\ -m) \tag{A7a}$$

and

$$C(111;000)=0, \tag{A7b}$$

we conclude that

$$\langle\vec{J}(11)\rangle=0. \tag{A8}$$

Using the same reasoning as above, we can also show that

$$\langle\vec{J}(22)\rangle=0. \tag{A9}$$

The expectation values of the operator $\vec{J}(21)$ can be written as

$$\langle\vec{J}(21)\rangle=\mathrm{Tr}[\rho\vec{J}(21)]=\sum_{mm'}\langle 1m|\rho|2m'\rangle\langle 2m'|\vec{J}|1m\rangle. \tag{A10}$$

If we assume that coherence exists only between levels $|F=1;\ m=0\rangle$ and $|F=2;m=0\rangle$ we can write for $\langle\vec{J}(21)\rangle$,

$$\langle\vec{J}(21)\rangle=\langle 10|\rho|20\rangle\langle 20|J_z|10\rangle\hat{e}_z. \tag{A11}$$

Similarly, one can also write for $\langle\vec{J}(12)\rangle$,

$$\langle J(12)\rangle=\langle 20|\rho|10\rangle\langle 10|J_z|20\rangle\hat{e}_z. \tag{A12}$$

The matrix element $\langle 20|J_z|10\rangle$ can be evaulated using the Wigner–Eckart theorem

$$\langle IJ20|J_z|IJ10\rangle=(-1)^{I-J}C(112;000)[(2J+1)3]^{1/2}\times W(J1J2;I1)\times[J(J+1)]^{1/2}. \tag{A13}$$

The Clebsch–Gordan and Racah coefficients in (A13) can be evaluated to give $C(112;000)=\sqrt{\frac{2}{3}}$ and $W(\frac{1}{2}1\frac{1}{2}2;\frac{3}{2}1)=1/\sqrt{12}$.

Thus we obtain

$$\langle 20|J_z|10\rangle=-\tfrac{1}{2}. \tag{A14}$$

In a similar way, we can evaluate $\langle 10|J_z|20\rangle$ to give

$$\langle 10|J_z|20\rangle=-\tfrac{1}{2}. \tag{A15}$$

Substituting (A14) in (A11), and (A15) in (A12), we obtain

$$\langle\vec{J}(21)\rangle=-\tfrac{1}{2}\langle 10|\rho|20\rangle\hat{e}_z \tag{A16a}$$

and

$$\langle\vec{J}(12)\rangle=-\tfrac{1}{2}\langle 20|\rho|10\rangle\hat{e}_z. \tag{A16b}$$

APPENDIX B: EVALUATION OF $\langle Q(FF')\rangle$ FOR Rb^{87} GROUND STATE

The definition of the quadrupole operator $\overleftrightarrow{Q}(FF')$ is given in MTH (58) as

$$\overleftrightarrow{Q}(FF')=\sum_M(-1)^M\overleftrightarrow{Q}_{2M}T_{2-M}(FF'), \tag{B1}$$

where $\overleftrightarrow{Q}_{2M}$ is an irreducible basis dyadic defined by HM (A10) and $T_{2-M}(FF')$ is an irreducible basis operator defined by HM (A1). The expectation value of $\overleftrightarrow{Q}(11)$ is

$$\langle\overleftrightarrow{Q}(11)\rangle=\mathrm{Tr}[\rho\overleftrightarrow{Q}(11)]=\sum_{Fm}\langle Fm|\rho\overleftrightarrow{Q}(11)|Fm\rangle=\sum_{mm'}\langle 1m|\rho|1m'\rangle\langle 1m'|\overleftrightarrow{Q}(11)|1m\rangle. \tag{B2}$$

We assume there are no coherences or population difference between the Zeeman sublevels within the $F=1$ hfs level so we can write (B2) as

$$\langle\overleftrightarrow{Q}(11)\rangle=\langle 11|\rho|11\rangle\sum_m\langle 1m|\overleftrightarrow{Q}(11)|1m\rangle. \tag{B3}$$

From the definition in (B1) we can write the matrix element $\langle 1m|\overleftrightarrow{Q}(11)|1m\rangle$ as

$$\langle 1m|\overleftrightarrow{Q}(11)|1m\rangle=\overleftrightarrow{Q}_{20}\langle 1m|T_{20}(11)|1m\rangle. \tag{B4}$$

According to HM (A1) the matrix element of the basis operator may be written as

$$\langle 1m|T_{20}(11)|1m\rangle=(-1)^{m-1}C(112;m\ 0\ m). \tag{B5}$$

Substituting (B4) and (B5) in (B3) we write for $\langle\overleftrightarrow{Q}(11)\rangle$,

$$\langle\overleftrightarrow{Q}(11)\rangle=\langle 11|\rho|11\rangle\overleftrightarrow{Q}_{20}\sum_m(-1)^{m-1}C(112;m\ 0\ m). \tag{B6}$$

The sum in (B6) can be shown to vanish. Therefore, we conclude

$$\langle\overleftrightarrow{Q}(11)\rangle=0. \tag{B7}$$

Using the same reasoning as above, we can also show that

$$\langle\overleftrightarrow{Q}(22)\rangle=0. \tag{B8}$$

The expectation value of the quadrupole operator $\overleftrightarrow{Q}(12)$ is

$$\langle Q(12)\rangle=\mathrm{Tr}[\rho\overleftrightarrow{Q}(12)]=\sum_{mm'}\langle 2m|\rho|1m'\rangle\langle 1m'|\overleftrightarrow{Q}(12)|2m\rangle. \tag{B9}$$

Since coherence exists only between the $|F=1;\ m=0\rangle$ and $|F=2;m=0\rangle$ levels, the only nonvanishing off-diagonal density matrix elements are $\langle 20|\rho|10\rangle$ and $\langle 10|\rho|20\rangle$. Hence, we can write for $\langle\overleftrightarrow{Q}(12)\rangle$,

$$\langle\overleftrightarrow{Q}(12)\rangle=\langle 10|\overleftrightarrow{Q}(12)|20\rangle\langle 20|\rho|10\rangle. \tag{B10}$$

Similarly, we can show that the expectation value of $\overleftrightarrow{Q}(21)$ can be written as

$$\langle\overleftrightarrow{Q}(21)\rangle = \langle 20|\overleftrightarrow{Q}(21)|10\rangle\langle 10|\rho|20\rangle. \quad \text{(B11)}$$

Using the definition given in (B1) we can write

$$\langle 20|\overleftrightarrow{Q}(12)|10\rangle = \overleftrightarrow{Q}_{20}\langle 20|T_{20}(12)|10\rangle. \quad \text{(B12)}$$

From the definition of T_{2M} given in HM (A1), we find that

$$\langle 20|T_{20}(12)|10\rangle = -C(212;000) = 0. \quad \text{(B13)}$$

Therefore, substituting (B13) and (B12) in (B10) we conclude that

$$\langle\overleftrightarrow{Q}(12)\rangle = 0. \quad \text{(B14)}$$

Similarly, the matrix element $\langle 20|\overleftrightarrow{Q}(21)|10\rangle$ in (B11) can be written as

$$\langle 20|\overleftrightarrow{Q}(21)|10\rangle = \overleftrightarrow{Q}_{20}\langle 10|T_{10}(21)|20\rangle. \quad \text{(B15)}$$

Once again from the definition of T_{LM} we can write

$$\langle 10|T_{20}(21)|20\rangle = -C(122;000) = 0. \quad \text{(B16)}$$

Substituting (B16) and (B17) in (B11), we also conclude that

$$\langle\overleftrightarrow{Q}(21)\rangle = 0. \quad \text{(B17)}$$

---

*Work supported in part by the Joint Services Electronics Program (U. S. Army, U. S. Navy, and U. S. Air Force) under Contract No. DAAB07-69-C-0383, and in part by the U. S. Air Force Office of Scientific Research under Contract No. AFOSR-68-1454B.

[1]H. G. Dehmelt, Phys. Rev. **105**, 1924 (1957).
[2]W. E. Bell and A. L. Bloom, Phys. Rev. **107**, 1559 (1957).
[3]A. H. Firester and T. R. Carver, Phys. Rev. Lett. **17**, 947 (1966).
[4]B. S. Mathur, H. Y. S. Tang, R. Bulos, and W. Happer, Phys. Rev. Lett. **12**, 1035 (1968).
[5]R. C. Miller and N. Wittwer, IEEE J. Quantum Electron. **QE-1**, 49 (1965).
[6]H. Tang and W. Happer, Phys. Rev. Lett. **24**, 551 (1970).
[7]B. S. Mathur, H. Tang, and W. Happer, Phys. Rev. A **2**, 648 (1970).
[8]W. Happer and B. S. Mathur, Phys. Rev. **163**, 12 (1967).
[9]W. Happer and B. S. Mathur, Phys. Rev. **163**, 16 (1967).
[10]W. Happer and B. S. Mathur, Phys. Rev. **163**, 17 (1967).
[11]J. P. Barrat and C. Cohen-Tannoudji, J. Phys. Radium **22**, 329 (1961); J. Phys. Radium **22**, 443 (1961).
[12]W. Happer and B. S. Mathur, Phys. Rev. **163**, 13 (1967).
[13]W. E. Bell and A. L. Bloom, Phys. Rev. Lett. **6**, 280 (1961).
[14]W. Happer and B. S. Mathur, Phys. Rev. Lett. **18**, 727 (1967).
[15]We will assume for simplicity that the optical-pumping light is uniform throughout the vapor. Further discussion of this point will be given in Sec. III with regard to phasematching.
[16]F. Grossetête, J. Phys. (Paris) **25**, 383 (1964).
[17]H. M. Gibbs, Phys. Rev. A **3**, 500 (1971).
[18]M. Bouchiat and F. Grossetête, J. Phys. (Paris) **27**, 353 (1966).
[19]M. A. Bouchiat and J. Brossel, C.R. Acad. Sci. (Paris) **254**, 3650 (1962).
[20]A. H. Firester and T. R. Carver, Phys. Rev. Lett. **17**, 947 (1966).
[21]B. S. Mathur, H. Y. S. Tang, R. Bulos, and W. Happer, Phys. Rev. Lett. **12**, 1035 (1968).
[22]T. J. Killian, Phys. Rev. **27**, 578 (1926).
[23]Trade Name for low loss plastic foam obtained from Emerson & Cumming, Inc., Canton, Mass.
[24]B. S. Mathur, H. Tang, and W. Happer, Phys. Rev. **171**, 11 (1968).
[25]D. A. McGillis and L. Krause, Phys. Rev. **153**, 44 (1967); L. Krause, Appl. Opt. **5**, 1375 (1966).
[26]H. M. Gibbs and R. J. Hull, Phys. Rev. **181**, 214 (1969).
[27]Trade name for long chain paraffin.
[28]H. M. Gibbs and R. J. Hull, Phys. Rev. **181**, 153 (1969).
[29]W. Raith, Z. Phys. **163**, 197 (1961).

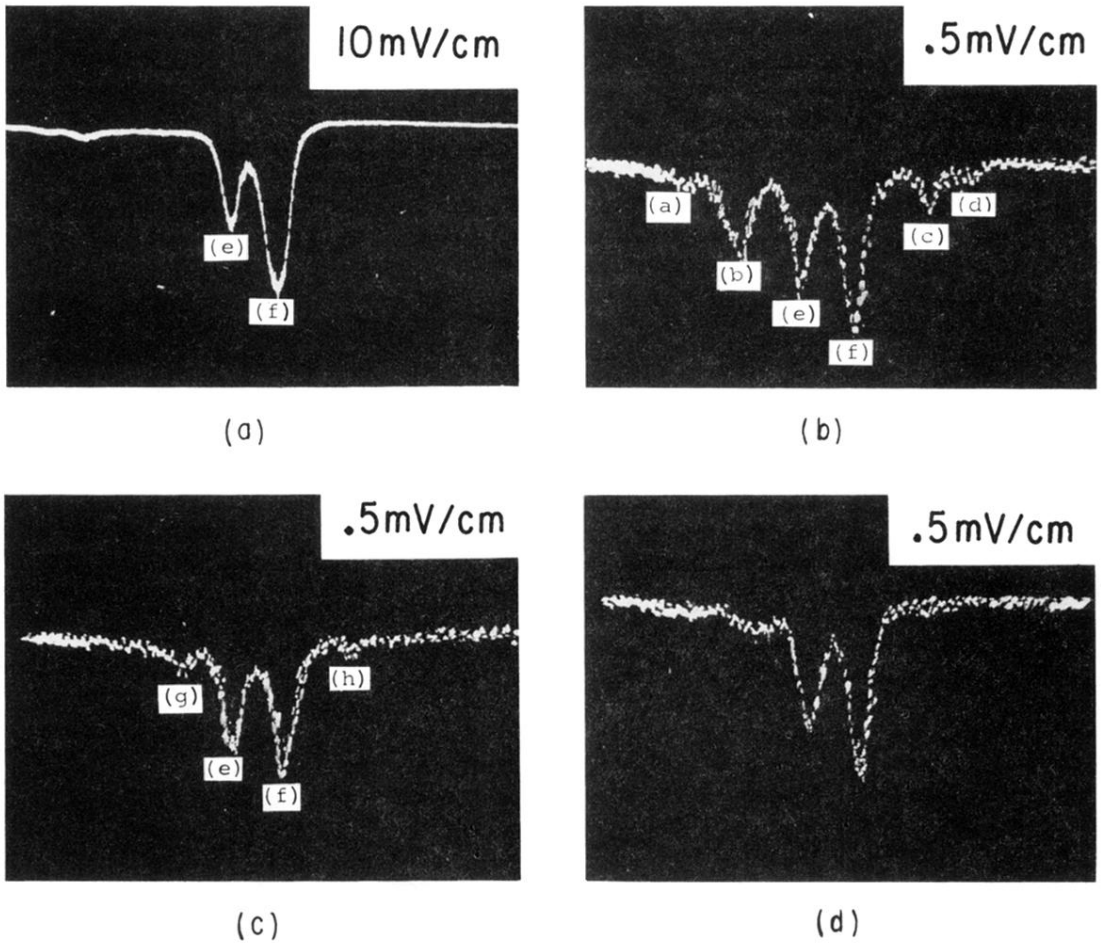

FIG. 13. (a) Oscillogram of the photomultiplier output when the polarizers P_1 and P_2 were parallel. (b) Oscillogram of the photomultiplier output when the polarizers P_1 and P_2 were crossed. (c) Oscillogram of the photomultiplier output when the polarizers P_1 and P_2 were crossed but the carrier light was removed. (d) Oscillogram of the photomultiplier output when the polarizers P_1 and P_2 were crossed but the microwave frequency was off resonance.